

POLITECNICO DI TORINO

MASTER DEGREE THESIS

Department of Control and Computer Engineering

Mechatronic Engineering

a.y. 2023/2024



**Politecnico
di Torino**

Study of flexible PCB coils in haptic applications

Supervisors:

Alessandro RIZZO
(Politecnico di Torino - DET)

Domenico PRATTICIZZO
(Università di Siena - DIISM -
SIRSLab)

Leonardo FRANCO
(Università di Siena - DIISM -
SIRSLab)

Candidate:

Morgan CASALE

June 2024

POLITECNICO DI TORINO

Abstract

Department of Control and Computer Engineering
Mechatronic Engineering

Study of flexible PCB coils in haptic applications

by Morgan CASALE

As the number of in-orbit satellites increases, the need for a way to service them becomes increasingly critical.

Recently the EU funded EROSS, a project with the purpose of providing a new range of services for in orbit satellites with consequent analysis for satellite design and life-cycle management. This initiative aims to enhance the availability of cost-effective and secure orbital services by assessing and validating the essential technological components of the Servicer spacecraft. The incorporation of robotic space technologies working on this project will lead to greater autonomy and safety in executing these services in space, requiring reduced ground-based supervision.

This master's thesis presents an innovative approach to pose estimation using deep learning and computer vision techniques. The research explores the development and implementation of a system for in-orbit satellites pose estimation. Delving into the complexities of rendezvous maneuvers, the system devised herein addresses the challenges associated with achieving and maintaining accurate pose estimations in the ever-changing and demanding conditions of space. Through a comprehensive exploration, this thesis contributes valuable insights and practical solutions to enhance the reliability and efficiency of satellite rendezvous processes.

A mono camera system is employed, reducing the hardware complexity and costs while maintaining performance. The camera captures pictures of the target satellite during the whole approach phase. A deep learning framework, based on a Convolutional Neural Network (CNN), is used to identify and track landmark features on the target satellite from captured images. This CNN-based approach provides high accuracy in feature recognition and tracking precision. A neural network-based regression model is introduced to map the 2D image coordinates or identified landmarks to their corresponding 3D coordinates with respect to the camera frame. This implementation permits to have a mono-camera instead of a stereo-camera system. Finally, incorporating the CPD algorithm, the system aligns the predicted 3D point clouds to the reference model, enabling accurate pose estimation and tracking.

The proposed system is tested through simulations. The results demonstrate the system's capability to estimate the pose of in-orbit satellites. This research contributes to the advancement of autonomous satellite operations, space debris management, and space exploration. Furthermore, it has the potential to enhance satellite rendezvous and capture capabilities.

Contents

Abstract	i
1 Introduction	1
1.1 Thesis objective	1
1.2 Necessary background (?)	2
1.3 Thesis structure	2
2 Background	4
2.1 Magnetic Coils	4
2.1.1 Brief History	4
2.1.2 Physics of an inductor?	4
Inductance	4
Reactance	5
Joule heating	6
Definition of Root Mean Square (RMS) values	6
2.1.3 Magnetic field generation	6
Magnetic Flux and Field relation	8
2.2 PCB Coils	8
2.2.1 Planar coils	8
2.2.2 Planar coil magnetic field	9
2.2.3 Multi-layer PCB coils	10
Total inductance	11
Magnetic field generated by a Multilayer coil	12
2.3 Flexible PCB coils	12
2.3.1 Pros of flexible coils	12
2.3.2 Application challenges	13
Rise of high resistance	13
Joule effect	14
Magnetic field strength	15
Resistance parasitic effects due to AC current	15
2.3.3 Running flexible PCB coils	18
High current needs	18
Constant Voltage vs Constant Current power supplying	19
2.4 Modelling of the Entire System	19
2.4.1 Neodymium magnets (magnetic strength wrt class and dimensions)	20
2.4.2 Magnetic force between magnet and coil	20
2.4.3 Membrane-magnet system	22
Membrane stiffness	22
Membrane damping	25
2.4.4 Finger grasping model	25

3 Overview of Haptic Feedback	28
3.1 Physics of Haptic Feedback	28
3.1.1 Biology of Haptic Sensing	28
3.1.2 Haptic sensitivity	29
3.2 State of the Art in vibrotactile haptic feedback	30
3.2.1 Piezoelectric actuators	30
Frequency response	30
Force performances	31
Power consumption	31
3.2.2 Texture rendering	31
4 Powering circuit design	32
4.1 Power Circuit Block diagram	32
4.2 Controller	32
4.2.1 ESP32 DAC Characteristics	33
4.2.2 ESP32 waveform generator	33
4.3 Signal Conditioning Circuit	33
4.4 Amplifier circuit	34
4.4.1 Power Operational Amplifiers	34
Power op-amp characteristics	35
Power dissipation problems	35
4.4.2 High Power Voltage Amplifier	35
Noise filtering	36
5 Implementation and Prototypes	38
5.1 Coils alternatives	38
5.1.1 Dresda coils	38
Low resistance and high power needs	38
Low magnetic field strength	38
Fragility and low flexibility	40
5.1.2 Flexar coils	40
Lower resistance and power needs	40
Higher magnetic field strength	41
Higher flexibility	42
5.2 Rigid Prototypes	42
5.2.1 1st version - Dresda Coils testbed	42
Flexible magnetic membrane	42
Adjustable height platform for coil and membrane	42
Prototype usability	43
5.2.2 Wearable Rigid Prototypes	43
Finger-Membrane interface	44
Sleeve production	45
Keep the distance from the coil	46
Heat dissipation	48
Prototype usability	48
5.3 Flexible Mat Prototypes	48
5.3.1 Design of the membrane	48
Material stiffness and thickness	49
Membrane structure vs magnet dimensions	49
5.3.2 Design of the mat	50
Magnet chamber and membrane	51

Distance magnet-coil	53
Coil trap	53
Production method	53
5.3.3 Design faults and problems	55
Membrane fragility	55
Overall system flexibility	56
Coil trap design faults	56
5.4 Experimentation and Evaluation	57
5.4.1 Heating testing	57
Single coil in DC	57
Single coil in AC [-V, V]	57
Single coil in AC [0, V]	57
Two coils in parallel DC	57
Two coils in parallel AC	57
5.4.2 Magnet size vs Force	57
5.4.3 Force vs number of coils	57
5.4.4 Voltage vs Force	57
6 Discussion and conclusions	58
6.1 Challenges in On-Board AI Systems for Space Missions	58
6.1.1 Verifiability Issues	58
6.1.2 Computational Issues	58
6.2 Results Analysis	59
6.3 Possible Improvements	59
6.3.1 Landmark Mapping Sensitivity	59
6.4 Conclusions	60
A Support Code	61
A.1 Ground Truth Heatmaps	61
A.2 Landmark Location Selection	62
Bibliography	63
Acknowledgements	65

List of Figures

2.1	RMS values for different waveforms.	7
2.2	Magnetic field generated by a solenoid.	7
2.3	Internal structure of a planar coil.	9
2.4	Coils Shapes	9
2.5	Spiral magn field	10
2.6	Coil spiral	11
2.7	Power profile of a Flexar coil	15
2.8	Flexar magnetic field profile	16
2.9	Skin depth	16
2.10	Fskin of Flexar	18
2.11	Skin effect on thicker traces	18
2.12	Proximity effect	19
2.13	Bond graph of the coil-magnet-membrane system.	20
2.14	Coil-Magnet position	21
2.15	Coil-Magnet Transducer bond graph.	22
2.16	Membrane structure	23
2.17	Membrane mat	23
2.18	Bond graph of the membrane-magnet system.	24
2.19	Membrane structure simplified as two fixed beams.	24
2.20	Final mechanical bond-graph of the membrane and magnet.	26
2.21	Model of two soft fingers grasping the object.	26
2.22	Bond graph of the finger grasping model.	27
3.1	Vibrotactile Sensitivity as a function of the applied pressure force.	30
4.1	Block diagram of the power circuit.	32
4.2	ESP32 16Hz Sine wave generated by the ESP32 Signal Generator software.	33
4.3	Signal conditioning circuit.	34
4.4	Power Op Amp block diagram.	35
4.5	Inverting amplifier circuit.	36
4.6	Inverting amplifier circuit with low-pass filter.	36
4.7	Picture of the implemented power stage.	37
5.1	Dresden coil [5]	39
5.2	Power profile of the Dresden coil	39
5.3	Magnetic field produced by the Dresden coil	39
5.4	Flexar coil	40
5.5	Power profile of the Flexar coil	41
5.6	Magnetic field produced by the Flexar coil	41
5.7	Dresden coil HZDR test setup	42
5.8	Finger platform	43
5.9	Adjustable platform	43

5.10 Finger silicon sleeve front and back view	44
5.11 Mold cavity	45
5.12 Mold core	45
5.13 Explode of the complete silicon finger sleeve holder	46
5.14 Silicon finger sleeve holder	47
5.15 Explode of the coil trap	47
5.16 Bottom and top view of the real prototype	48
5.17 Membrane virtual model of the small magnet prototype.	49
5.18 Membrane cross-section of the small magnet prototype (t->thickness, L->length).	50
5.19 Membrane cross-section of the big magnet prototype.	50
5.20 Flexible mat mold cavity	51
5.21 Assembly of the mold core	52
5.22 Mold core center.	52
5.23 Coil trap model.	54
5.24 Coil trap placed inside the mat.	54
5.25 Complete mold for the mat.	55
5.26 Flexible mat prototype bending.	56
5.27 Coil trap separating when the mat is bent.	56

List of Tables

2.1	Physical characteristics of a Flexar coil	14
2.2	Magnetic field remanence of different N grade neodymium magnets. .	21

List of Abbreviations

PCB	Printed Circuit Board
AC	Alternated Current
DC	Direct Current
AI	Artificial Intelligence
CAD	Computer-Aided Design
CNN	Convolutional Neural Network
CPD	Coherent Point Drift
CV	Computer Vision
D	Dimension(s)
DOF	Degrees Of Freedom
EM	Expectation-Maximization
EROSS	European Robotic Orbital Support Services
EU	European Union
FAIR	Facebook's AI Research lab
FOV	Field Of View
GEO	Geostationary Equatorial Orbit
GMM	Gaussian Mixture Model
GPU	Graphics Processing Unit
HRNet	High-Resolution Network
ICP	Iterative Closest Point
IOD	In Orbit Demonstration
LEO	Low Earth Orbit
ML	Machine Learning
MSE	Mean Squared Error
NN	Neural Network
RANSAC	Random Sample Consensus
R-CNN	Region-based Convolutional Neural Network
RPY	Roll, Pitch, Yaw
SIFT	Scale Invariant Feature Transform
SURF	Speeded Up Robust Feature
MSER	Maximally Stable Extremal Regions
BRIEF	Binary Robust Independent Elementary Features
PnP	Perspective-n-Point
SfM	Structure from Motion
SPN	Spacecraft Pose Network
SWaP	Size Weight and Power

List of Symbols

Symbol	Name	Unit
E_{CNN}	Landmark Regression error	px
E_{NN}	Landmark Mapping error	cm
E_T	Translation error	cm
E_R	Rotation error	°
S_T	Translation score	-
S_R	Rotation error	rad

Chapter 1

Introduction

1.1 Thesis objective

In the expanse of space, satellite missions and on-orbit services have become critical assets, serving a myriad of applications including Earth observation, global communication, and scientific research.

The progressive introduction of AI algorithms into various environments, including space applications, represents a significant leap forward in technological advancement. In the context of pose estimation in space, the incorporation of AI brings a multitude of benefits that enhance the autonomy of satellite operations.

In recent years, we've witnessed a rapid proliferation of on-orbit satellites, driven by advancements in technology and the need for enhanced space services. As the number of these satellites continues to rise, the complexities associated with their safe and effective navigation, rendezvous, and scientific missions have grown in tandem. This is where AI shines, as it steps in to revolutionize the field of satellite pose estimation.

AI algorithms, equipped with their machine learning capabilities, enable satellites to process vast amounts of data from onboard sensors with remarkable precision and efficiency. This means an elevated level of accuracy in determining a satellite's position, orientation, and trajectory. But the benefits go beyond mere precision.

AI algorithms, equipped with their machine learning capabilities, enable satellites to process vast amounts of data from onboard sensors with remarkable precision and efficiency. One remarkable development is the ability to estimate a satellite's position and orientation using just a single camera, eliminating the need for a stereocamera setup. This innovation not only enhances accuracy but also reduces hardware complexity, making satellite design more cost-effective. AI-driven monocular camera-based pose estimation empowers satellites to autonomously process visual data, adjust to dynamic orbital environments, and make informed decisions, even in the midst of complex maneuvers, ensuring the mission's success and safety.

Moreover, the increased autonomy provided by AI minimizes the need for constant human intervention and ground control. This not only reduces operational costs but also allows human operators to focus on more strategic aspects of the mission, enhancing productivity and mission efficiency. As we look to the future, AI algorithms promise to usher in a new era of space exploration and satellite operations.

In summary, the progressive introduction of AI algorithms in space applications, particularly in pose estimation, opens the door to enhanced accuracy, real-time adaptability, autonomy, and overall mission efficiency. This transformative technology propels us closer to unlocking the full potential of space exploration and satellite services.

The objective of this thesis is to implement the rendezvous of a collaborative satellite using AI algorithms, with a particular emphasis on their applications in mono camera-based visual pose estimation. The focus is specifically directed towards a detailed analysis of rendezvous operations within the 200-20cm distance range from a non-cooperative satellite. This project delves into the critical aspects of pose estimation throughout the entire trajectory of the rendezvous process, extending from the initial approach to the final berthing phase.

1.2 Necessary background (?)

1.3 Thesis structure

The thesis is structured in further five chapters:

Chapter 2 - Background:

This chapter provides a comprehensive overview of key concepts necessary for the correct understanding of this work, with a focus on monocular camera models, perspective projection, pose estimation, and a general introduction to deep learning models.

Chapter 3 - State-of-art:

This chapter delves into monocular pose estimation methods, covering classic approaches like RANSAC and SfM, and exploring modern techniques such as end-to-end learning with networks like PoseNet and Mask R-CNN. The chapter also introduces feature learning, emphasizing CNN-based methods like HRNet for predicting 2D landmark locations. Moreover, some studies about spacecraft pose estimation and their use of deep learning architectures are presented. The chapter also delves into point set alignments, highlighting the widely used and advanced algorithms like Coherent Point Drift (CPD) technique employed in the method for final pose estimation.

Chapter 4 - Algorithms and Methods:

This chapter delves into the methodology's core algorithms and techniques. It outlines the offline architecture, detailing the 2D-3D correspondence process, landmark regression, and the neural network-based landmark mapping. The chapter then presents the online architecture, covering real-time processing and the Coherent Point Drift technique for pose estimation. Implementation challenges and dataset considerations are also discussed, providing a comprehensive overview of the applied methods.

Chapter 5 - Implementation and Experiments:

This chapter presents the tools and technologies employed for the project implementation and the evaluation metrics for pose estimation, Landmark Regression, Landmark Mapping are described. The chapter culminates in the

assessment of both training and test datasets, showcasing the method's robustness and generalization across diverse scenarios. Overall, it provides comprehensive exploration of the research's implementation and experimentation phases.

Chapter 6 - Discussions and Conclusions:

The Chapter delves into challenges faced by on-board AI systems in space missions, focusing on verifiability and computational load. It emphasizes the significance of minimizing translation errors for accurate maneuvering in the proposed multi-model configuration. The section explores potential improvements, including enhanced landmark selection and strategies to fortify system robustness.

Chapter 2

Background

2.1 Magnetic Coils

2.1.1 Brief History

The connection between electricity and magnetism was first demonstrated by Hans Christian Oersted in 1820 when he observed that an electric current flowing through a wire could deflect a nearby magnetic needle.

Meanwhile, the creation of the first practical electromagnet is credited to William Sturgeon and André-Marie Ampère who after Oersted's discovery experimented with creating coil windings wrapped around an iron core which allowed them to achieve much stronger magnetic fields.

During the 1830's Michael Faraday's discovery of electromagnetic induction further advanced the understanding of magnetic fields and coils. Faraday demonstrated that a changing magnetic field could induce an electric current in a nearby conductor, laying the groundwork for transformers and modern electrical generators.

The latter half of the 19th century saw rapid advancements in electrical engineering. Innovations like early electric generators (dynamos), transformers, and electric motors heavily relied on magnetic coils for their operation. Researchers such as Nikola Tesla and Thomas Edison further developed these technologies.

Magnetic coils continue to play a vital role in various fields, including power generation, telecommunications, electronics, and medical imaging (such as MRI machines). With advancements in materials science and manufacturing techniques, magnetic coils have become more efficient, compact, and versatile.

In recent years, as the use of PCBs has become widespread, researchers started experimenting with creating coil windings utilizing this technology.

2.1.2 Physics of an inductor?

Inductance

All conductors have some inductance, which may have either desirable or detrimental effects in practical electrical devices. The inductance of a circuit depends on the geometry of the current path and the magnetic permeability of nearby materials.

Any alteration to a circuit that increases the flux (total magnetic field) through the circuit produced by a given current increases the inductance, because inductance is equal to the ratio of magnetic flux to current

$$L = \frac{\Phi(i)}{i} \quad (2.1)$$

Where:

- L is the inductance [H].
- i is the current [A].
- $\Phi(i)$ is the magnetic flux through the circuit [Wb].

Reactance

When a current signal is applied to an inductor, a flux is generated and, considering Faraday's law of induction, any change in flux through a circuit induces an electro-motive force \mathcal{E} , proportional to the rate of change of flux

$$\mathcal{E} = -L \frac{d\Phi(t)}{dt} \quad (2.2)$$

Then using Lenz's law, the voltage across the inductor is given by

$$V = -L \frac{di}{dt} \quad (2.3)$$

Inductors resist changes in current due to the magnetic field they generate when current passes through them. When we apply a sinusoidal signal to our inductor, the current will be continuously changing direction. The inductor's opposition to these changes is represented as reactance.

Inductive reactance (X_L) is measured in ohms and is calculated using the formula:

$$X_L = 2\pi f L \quad (2.4)$$

Where:

- X_L = Inductive reactance [Ω]
- f = Frequency of the AC current [Hz]
- L = Inductance of the inductor [H]

We can then calculate the total impedance of the inductor as

$$Z = \sqrt{R^2 + X_L^2} \quad (2.5)$$

Where:

- Z = Total impedance [Ω]
- R = Resistance of the inductor [Ω]
- X_L = Inductive reactance [Ω]

Joule heating

Inductors are passive components, meaning they do not generate energy. However, they do store energy in the form of a magnetic field. When the current through an inductor changes, the magnetic field changes, and energy is stored in the field. When the current decreases, the magnetic field collapses, and the energy is returned to the circuit. This energy is dissipated as heat in the inductor's windings.

The power dissipated in an inductor is given by the relation

$$P = |I_{RMS}|^2 R = \frac{|V_{RMS}|^2}{|Z|^2} R \quad (2.6)$$

Where:

- P = Power dissipated in the inductor [W]
- I = Current flowing through the inductor [A]
- R = Resistance of the inductor [Ω]
- V = Voltage across the inductor [V]
- Z = Total impedance of the inductor [Ω]

Definition of Root Mean Square (RMS) values

As we have seen in the previous paragraphs, the power dissipated by the coil depends on the root mean square values of the current and voltage. We use the RMS values because they allow us to compare the power dissipated by the coil when powered in AC and DC conditions. For DC signals these values are equal to the DC one, while for sinusoidal signals V_{RMS} can be calculated as

$$V_{RMS} = \sqrt{\frac{1}{T} \int_T^0 [f(t)]^2 dt} \quad (2.7)$$

Where:

- T is the period of the input signal
- $f(t)$ is the function of the signal

Then in case we're dealing with AC signals having a DC offset we can use the formula

$$V_{RMS_{AC+DC}} = \sqrt{V_{DC}^2 + V_{RMS_{AC}}^2} \quad (2.8)$$

Some formulas for important waveforms:

2.1.3 Magnetic field generation

The strength of the magnetic field on the z-axis of the coil is derived from the Biot-Savart Law and is given by the formula

$$B_z = \frac{N\mu_0 I r^2}{2(r^2 + z^2)^{\frac{3}{2}}} \quad (2.9)$$

Name	Waveform	V_{RMS}
DC	V_P	V_P
Sine Wave $[-V_P, V_P]$	$V_P \sin(2\pi f t)$	$\frac{V_P}{\sqrt{2}}$
Polarized Sine Wave $[0, V_P]$	$\frac{V_P}{2} (\sin(2\pi f t) + 1)$	$\frac{V_P}{2} \sqrt{\frac{3}{2}}$
Square Wave $[-V_P, V_P]$	$V_P \text{sgn}(\sin(2\pi f t))$	V_P
DC-shifted Square Wave $V_{DC} + [-V_P, V_P]$	$V_{DC} + V_P \text{sgn}(\sin(2\pi f t))$	$\sqrt{V_{DC}^2 + V_P^2}$

FIGURE 2.1: RMS values for different waveforms.

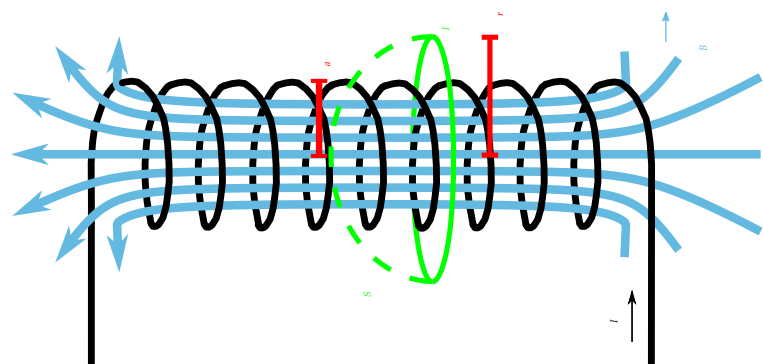


FIGURE 2.2: Magnetic field generated by a solenoid.

Where:

- B_z is the magnetic field on the z-axis [T].
- μ is the magnetic permeability of the medium [H/m].
- I is the current flowing through the wire [A].
- r is the radius of the coil [m].
- N is the number of turns of wire in the coil.
- z is the z-distance from the center of the coil [m].

If the coil lacks a core the permeability of free space is used instead of the core's permeability; instead if wound on a ferromagnetic core the permeability of the core is calculated as

$$\mu = \mu_0 \cdot \mu_r$$

where μ_r is the relative permeability of the core material.

With the right material for the core, the magnetic field intensity can be highly increased compared to the field generated by the coil alone.

Magnetic Flux and Field relation

We can also relate the magnetic field to the magnetic flux generated by the coil. The magnetic flux is given by the formula

$$\Phi_B = B \cdot A \quad (2.10)$$

Where:

- Φ_B is the magnetic flux [Wb].
- B is the magnetic field [T].
- A is the area of the coil [m^2].

2.2 PCB Coils

The biggest problem with standard coils is their size, especially in the z-direction as the more windings are used the thicker they will become. This is a problem for applications where space is limited, such as in the case of implantable devices. To address this issue, researchers have started to experiment with creating coil windings using PCB technology. This allows for the creation of coils that are thinner and more compact than traditional coils. In this section, we will discuss the different types of PCB coils and the challenges associated with their miniaturization.

2.2.1 Planar coils

As PCBs are 2D objects we can't work on the z-axis to create the coil's windings. This means that the windings have to be created on the same plane. In 1984 researchers from Osaka University proposed the first implementation of a possible solution in the form of planar coils. They proposed and tested a structure comprised of concentric spirals, with different shapes, made of a conductive material (mostly copper)

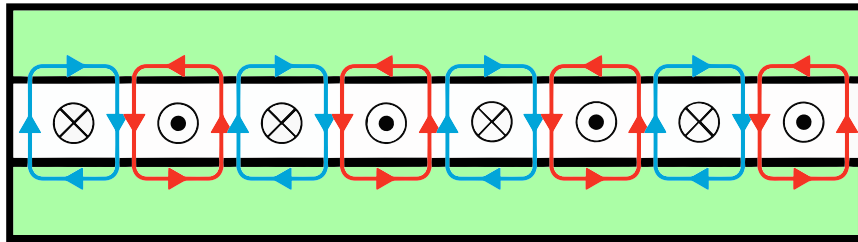


FIGURE 2.3: Internal structure of a planar coil.

suspended in an insulation material and then covered by two magnetic material layers (???) [7].

With the mainstream adoption of PCBs in the electronics industry, researchers have created planar coils using PCBs by etching spiral patterns on the copper layer. This allowed for the production of planar coils easily and cheaply.

The main advantage of planar coils is that they can be easily integrated into the PCB design, reducing the overall size of the device. This is particularly useful in the case of wireless power transfer systems, where the coils are used to transfer power between devices. The smaller size of the coils allows for more compact and portable devices.

Another advantage is the ability to design coils of arbitrary shapes and sizes, depending on the requirements of the application. This flexibility allows for the creation of coils that are optimized for specific applications and PCB shapes, resulting in improved performance.

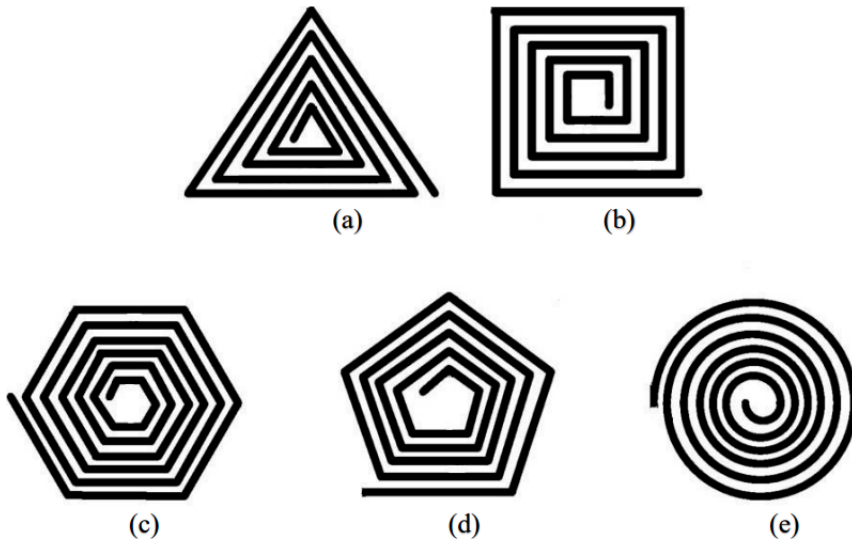


FIGURE 2.4: Different planar coil architectures such as (a) triangle, (b) square, (c) pentagon, (d) hexagon, (e) circle.

2.2.2 Planar coil magnetic field

The structure of a planar coil is very different from a standard one, as it is a flat structure with a spiral winding. The magnetic field generated by a planar coil is more complex than that of a standard coil, as the magnetic field is not concentrated

in the center of the coil but is distributed over the entire surface of the coil. The magnetic field generated by a planar coil is represented in Figure 2.5

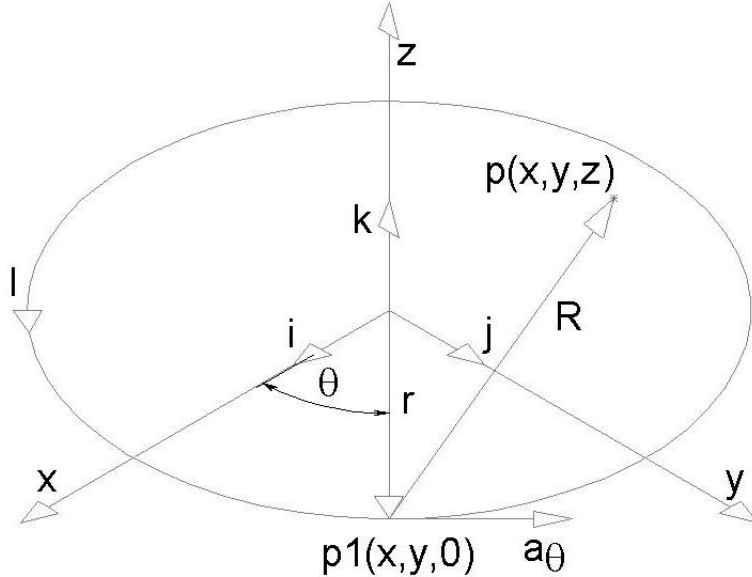


FIGURE 2.5: (c) Representation of the magnetic field generated by a circular spiral planar coil placed on an aluminum plate.[4]

Then considering again the circular spiral structure, the magnetic field generated by a planar coil at its surface can be derived as

$$B_z = \frac{\mu N I}{2} \cdot \frac{\ln(\frac{b}{a})}{b - a} \quad (2.11)$$

Where:

- B_z is the magnetic field on the z-axis [T]
- μ is the magnetic permeability of the medium [H/m]
- N is the number of turns of the spiral
- I is the current flowing through the wire [A]
- b is the external radius of the spiral [m]
- a is the internal radius of the spiral [m]

To then find the magnetic field at a distance z from the center of the coil, we can use the equation 2.9 from the previous subsection and substitute the radius r of the coil with

$$r' = \frac{b - a}{\ln \frac{b}{a}} \rightarrow B_z = \frac{\mu N I r'^2}{2(r'^2 + z^2)^{\frac{3}{2}}} \quad (2.12)$$

2.2.3 Multi-layer PCB coils

Another approach to miniaturizing PCB coils is to create multi-layer coils. This is done by stacking multiple layers of PCBs on top of each other, with each layer containing a different part of the coil. This allows for the creation of coils with a higher

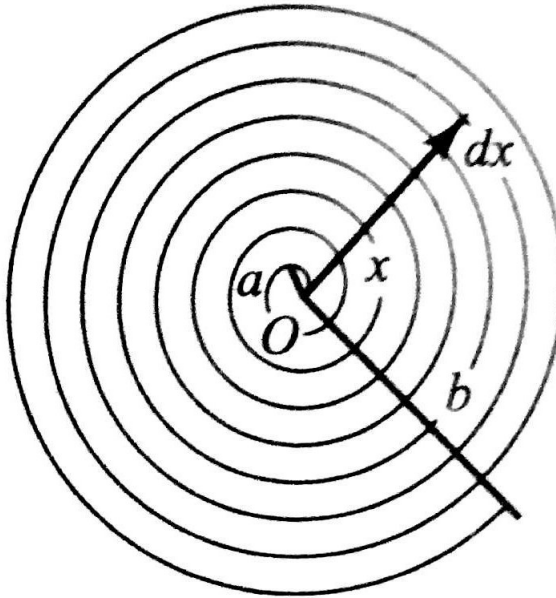


Fig. S2.75

FIGURE 2.6: Circular spiral coil.

number of windings in a smaller space. The main challenge with multi-layer PCB coils is the alignment of the different layers. If the layers are not aligned properly, the coil will not function correctly.

Current manufacturing allows for up to 10 layers of PCBs to be stacked on top of each other. However, the more layers that are added, the more difficult it becomes to align the layers correctly. If the layers are not aligned properly, the magnetic field generated by each layer will also not be aligned, which can lead to a decrease in the efficiency of the coil due to interferences.

Total inductance

Considering a two layers coil the total inductance can be calculated as

$$L_s = 2L_0 + 2M, M = K_c \cdot L_0 \quad (2.13)$$

Where:

- L_s is the total inductance of the coil [H].
- L_0 is the inductance of a single layer [H].
- M is the mutual inductance between the two layers [H].
- K_c is the coupling coefficient between the two layers.

Then K_c can be calculated with an empirical formula derived from multiple measurements by *Jonsenser Zhao* [22] as

$$K_c = \frac{N^2}{0.64[(0.184d^3 - 0.525d^2 + 1.038d + 1.001)(1.67N^2 - 5.84N + 65)]} \quad (2.14)$$

Where:

- N is the number of turns of the coil.
- d is the distance between the two layers [m].

Magnetic field generated by a Multilayer coil

We can use equation 2.1 and L_s calculated in the previous point to find the magnetic flux through the coils

$$\Phi(I) = L_s \cdot I \quad (2.15)$$

Then with equation 2.10 we can derive the total magnetic field as

$$B_t = \frac{L_s \cdot I}{\pi r^2} \quad (2.16)$$

Where:

- B_t is the total magnetic field [T].
- r is the radius of the coil [m].

2.3 Flexible PCB coils

Flexible PCB coils are a type of PCB coil that is made using a flexible substrate. This allows for the creation of coils that can be bent and twisted without breaking.

2.3.1 Pros of flexible coils

Flexible PCBs (Printed Circuit Boards) offer several advantages over traditional rigid PCBs. Here are some of the key pros of flexible PCBs:

1. **Flexibility and Space Savings:** Flexible PCBs can bend and twist, allowing for compact and efficient use of space in electronic devices.
2. **Lightweight:** The materials used in flexible PCBs are lightweight, making them ideal for applications where weight is a concern, such as in aerospace or portable electronics.
3. **Improved Design Freedom:** Flex PCBs allow for more creative and versatile designs because they can be formed into complex shapes and fit into tight or irregular spaces.
4. **Reduced Connectors and Interconnects:** Because flexible PCBs can bend, they can often eliminate the need for additional connectors and interconnects, reducing overall system complexity.
5. **Vibration and Shock Resistance:** Flexible PCBs can absorb shock and vibrations better than rigid PCBs, making them suitable for use in environments where these are concerns.

6. **Simplified Assembly:** With fewer connectors and interconnects, assembly becomes easier and faster, reducing labor and potential points of failure.
7. **High-Density Interconnects:** Flexible PCBs can support fine-pitch components and high-density interconnects, making them suitable for advanced electronics.

2.3.2 Application challenges

As said before flexible PCBs offer great design flexibility and the possibility of implementing innovative designs and devices but they also come with their own set of challenges; especially in the case of flexible coils.

Rise of high resistance

Taking as an example the flexible coil we'll be using in our project, the resistance of the coil is 30Ω . This is a relatively high resistance for a coil, especially when compared to traditional copper wire coils. This is due to the intrinsic structure of PCBs, especially flexible ones. PCBs are created by etching very thin copper traces on a substrate, in the case of flexible PCBs, as the substrate must be flexible, their thickness is even lower and consequently also the traces are.

The coil can be considered as a very long strand of a very thin copper so its resistance can be calculated using the Ohm Law

$$R = \rho \cdot \frac{L}{A} \quad (2.17)$$

Where:

- R is the resistance [Ω].
- ρ is the resistivity of the material [$\Omega \cdot m$].
- L is the length of the conductor [m].
- A is the cross-sectional area of the conductor [m^2].

Then to find the length of the copper traces we can use the approximated formula [20]

$$L = N\pi \frac{D + d}{2} \quad (2.18)$$

Where:

- N is the number of turns.
- D is the outer diameter of the coil [m].
- d is the inner diameter of the coil [m].

The tracks' cross-section is a rectangle so the area can be calculated as

$$A = w \cdot t \quad (2.19)$$

Where:

- w is the width of the track [m].

- t is the thickness of the copper [m].

Finally considering the physical characteristics of our coil

Coil Specifications	
Track (width/spacing)	$4/4\text{mil} = 1.016e - 4/1.016e - 4\text{m}$
Turns	$2*35$ (two coils in series)
External radius	$6.86e - 3\text{m}$
Copper thickness	$0.5oz = 1.74e - 5\text{m}$
Resistivity	$1.72e - 8\Omega\text{m}$
Maximum Constant Power	$0.8W$

TABLE 2.1: Physical characteristics of a Flexar coil

The Length of the tracks (considering both spires) will be $L = 3.4548\text{m}$ and the cross-section area will be $A = 1.7678e - 09\text{m}^2$. As we can observe we have a wire which is both very long and very thin so a high resistance is expected (from the calculation $R = 33.61\Omega$).

Also, the resistance of the coil is dependent on the Temperature of the coil, as the temperature increases the resistance of the copper increases as well. This is because the resistivity of copper increases with temperature. This is a problem as the coil releases a lot of heat when powered with high currents.

The temperature coefficient of resistivity of copper is $\alpha = 0.003862 \frac{1}{\circ C}$ so the resistivity of copper at a certain temperature can be calculated as

$$\rho(T) = \rho_{T_{ref}} \cdot (1 + \alpha \cdot (T - T_{ref})) \quad (2.20)$$

Where:

- $\rho_{T_{ref}}$ is the resistivity at the reference temperature [$\Omega \cdot m$].
- α is the temperature coefficient of resistivity [$\frac{1}{\circ C}$].
- T is the temperature [$\circ C$].
- T_{ref} is the reference temperature [20 $\circ C$].

Joule effect

As said before, a coil of this type releases a lot of heat when powered with high currents. This is also due to its high resistance. The heat dissipation of a coil can be calculated using the formula

$$P = I_{RMS}^2 R = \frac{V_{RMS}^2}{R} \quad (2.21)$$

Where:

- P is the power dissipated by the coil [W].
- I_{RMS} is the root mean square current [A].
- V_{RMS} is the root mean square voltage [V].

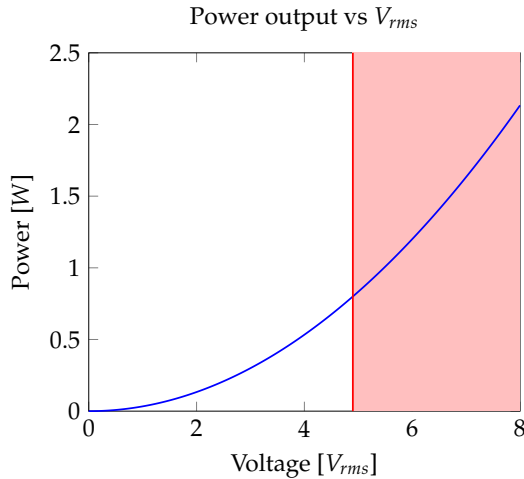


FIGURE 2.7: Power profile of a Flexar coil

- R is the resistance of the coil [Ω].

The coil can dissipate a maximum of 0.8W of power, this is a very low value and it is very easy to surpass it. This is a problem as the coil can be damaged if it dissipates more power than it can handle.

When exceeding the limit, even if the coil doesn't get damaged, the heat it releases can affect the performance of the coil. The coil's resistance increases with temperature, so the coil will dissipate even more power, this can lead to a thermal runaway situation where the coil will keep increasing its temperature until it gets damaged.

The only solution could be to introduce a heat sink to dissipate the heat but for the amount needed to be managed, we will show that flexible solutions aren't enough.

Magnetic field strength

As the coil can't be run at high currents, the magnetic field it generates will be very weak, this will affect the performance of the coil as the magnetic field is what allows the coil to interact with the environment. This is a problem as the coil will be less sensitive and will have a shorter range.

Considering the Flexar coil as an example we can plot the magnetic field strength, at the surface, as a function of the voltage applied to the coil using equation 2.11 (considering the coil as a parallel of two spirals)

As we can observe even at the power limit of 0.8W ($\simeq 5V$) the magnetic field generated by the coil is very low ($\simeq 4mT$).

Resistance parasitic effects due to AC current

This paragraph will be a brief introduction to the parasitic effects that can occur in a coil due to the AC current that flows through it. All these effects are negligible at low frequencies (up to about 1kHz) which is the range we are aiming for in this project, but we will explore them for the sake of future research.

The main parasitic effects that can occur in a coil are:

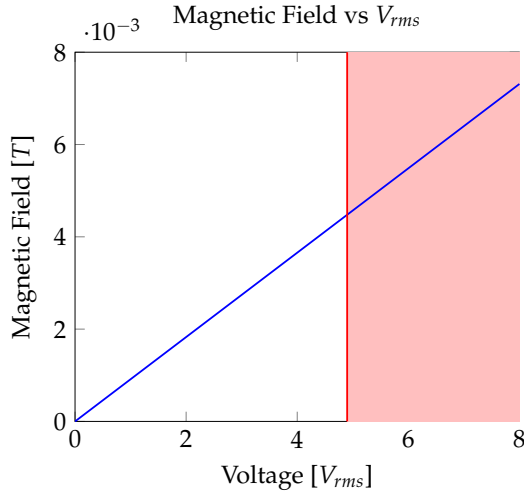


FIGURE 2.8: Flexar magnetic field profile

- **Reactance:** This is the opposition that a coil offers to the flow of AC current. This is due to the self-inductance of the coil which opposes the change in current flowing through it. This effect can lead to a change in the effective resistance of the coil.

The reactance of a coil can be calculated using the formula

$$X_L = 2\pi f L \quad (2.22)$$

Where:

- X_L is the reactance of the coil [Ω].
- f is the frequency of the AC current [Hz].
- L is the inductance of the coil [H].

Then the impedance of the coil can be calculated as

$$Z = \sqrt{R_{DC}^2 + X_L^2} \quad (2.23)$$

- **Skin effect:** This effect is due to the current flowing through a conductor tending to flow on the surface of the conductor. This gives rise to a thin layer inside the conductor where all the current flows. As a result, the effective resistance of the conductor increases. This effect is more pronounced at higher frequencies.

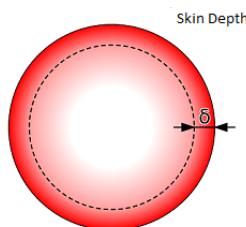


FIGURE 2.9: (c) Representation of the thin surface generated by the skin effect

The thickness of this area is called the **skin depth** and can be calculated using the formula

$$\delta = \sqrt{\frac{\rho}{\mu\pi f}} \quad (2.24)$$

Where:

- δ is the skin depth [m].
- ρ is the resistivity of the conductor [$\Omega \cdot m$].
- μ is the magnetic permeability of the medium [H/m].

The effective resistance of the conductor can be derived from the skin depth using Dowell's equation

$$R_{skin} = F_{skin} \cdot R_{DC} \quad (2.25)$$

and

$$F_{skin} = \frac{1}{2} \left(\frac{h}{\delta} \right) \frac{\sinh(\frac{h}{\delta}) + \sin(\frac{h}{\delta})}{\cosh(\frac{h}{\delta}) - \cos(\frac{h}{\delta})} \quad (2.26)$$

Where:

- R_{skin} is the effective resistance of the conductor due to the skin effect [Ω].
- F_{skin} is the skin effect factor.
- h is the thickness of the conductor [m].

In the case of the coil we're studying, the skin effect is negligible up to $1e8Hz$ as the thickness of the flexible PCB's traces is very low.

But we can observe from the study done on thicker traces' (0.5mm) coils that the skin effect starts to be already noticeable at $1e5Hz$.

- **Proximity effect:** This effect is similar to the skin effect but it occurs when two conductors are close to each other. The current flowing through one conductor induces an eddy current in the other conductor which can lead to a change in the effective resistance of the conductors.

The contribution of the proximity effect to the effective resistance of the coil can be calculated using the formula (considering current flowing in the coil $I_{ex} = 1A$) [12]

$$R_{proximity} = \frac{1}{12} h \sigma \pi^2 f^2 B_n^2 w^3 \quad (2.27)$$

Where:

- σ is the conductivity of the conductor [$\Omega^{-1} \cdot m^{-1}$].
- h is the thickness of the conductor [m].
- f is the frequency of the AC current [Hz].
- B_n is the average external magnetic field [T].
- w is the width of the conductor [m].

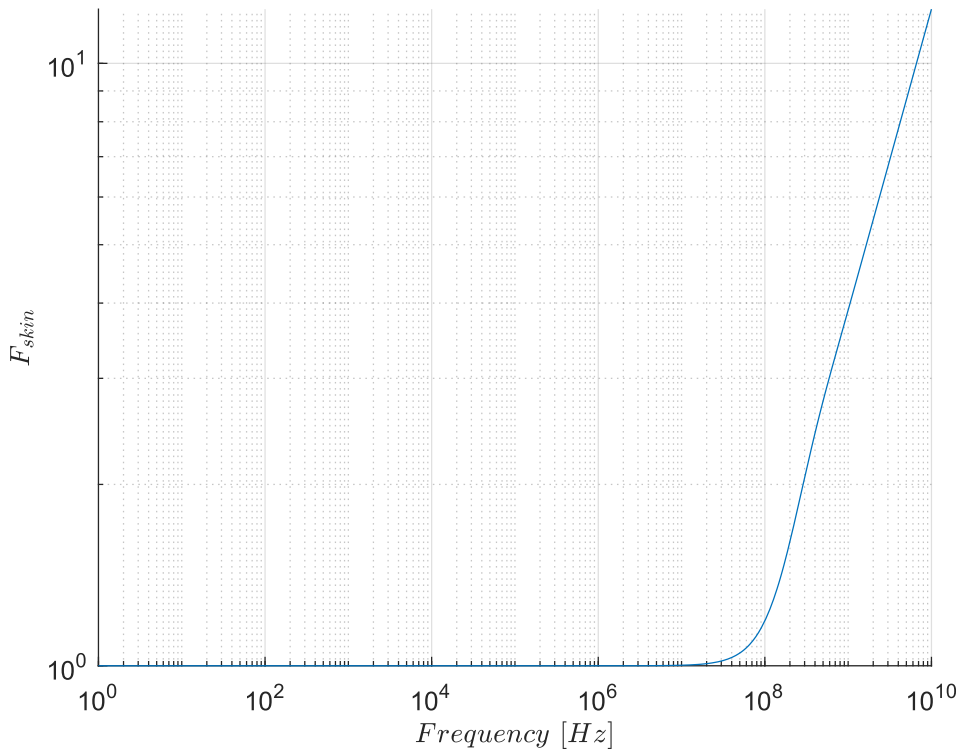


FIGURE 2.10: Logarithmic plot of the skin effect factor for a flexible PCB coil

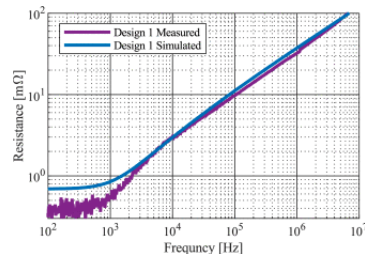


FIGURE 2.11: Skin effect on thicker traces [13]

We can also approximate $F_{proximity}$ ($F_{proximity} = R_{proximity} / R_{DC}$) as

$$F_{proximity} = \frac{F_{skin}}{3} \quad (2.28)$$

So when the contribution of the skin effect is negligible, the proximity effect will be negligible as well.

2.3.3 Running flexible PCB coils

High current needs

As discussed in the previous paragraph flexible coils have very high resistance so to produce even low magnetic fields high current must be provided. Considering the power limit of the Flexar coil $P_{max} = 0.8W$ we can calculate the maximum current

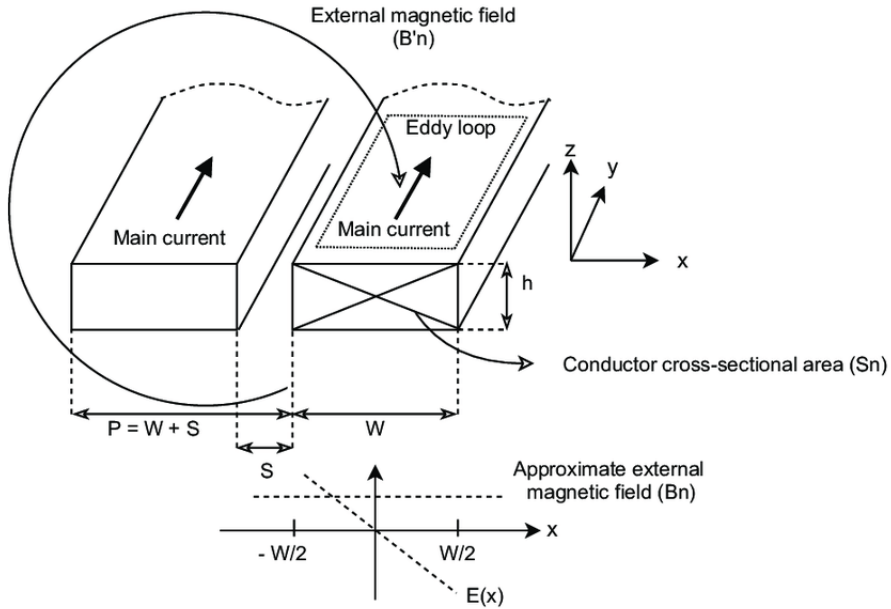


FIGURE 2.12: Representation of the proximity effect

that can be provided to the coil with 2.6 as

$$I = \sqrt{\frac{P_{max}}{R}} = \sqrt{\frac{0.8}{30}} = 0.1633A \quad (2.29)$$

Constant Voltage vs Constant Current power supplying

To power our coil we have two options, we can either provide a constant voltage or a constant current. Using a constant current source is not advisable due to the heating problem of the coil, at high currents as the coil is run it will heat up and its resistance will increase which will cause the power source to increase the voltage to keep the current constant. This in turn will cause the coil to heat up even more and the cycle will continue until the coil is damaged.

Instead, using a constant voltage source as the resistance increases due to the coil exceeding the heating and power threshold we will only have a decrease in the current which results in a loss of magnetic field strength but the coil won't get damaged.

2.4 Modelling of the Entire System

To be able to produce vibrations using the magnetic field produced by the coil we need to introduce to the system an object that can react to the magnetic field. As the magnetic field of the coil is very feeble we can use as the object Neodymium magnets, these are permanent magnets with a very strong internal magnetic field for their size. Using small ones and with the right pole facing the coil (same polarity as the generated magnetic field) it will be able to repel them and make them vibrate. Then to constrain the motion of the magnet and make it only move in the z -axis we have to add to the system a flexible membrane.

We can now model the entire system using a bond graph, as shown in figure 2.13.

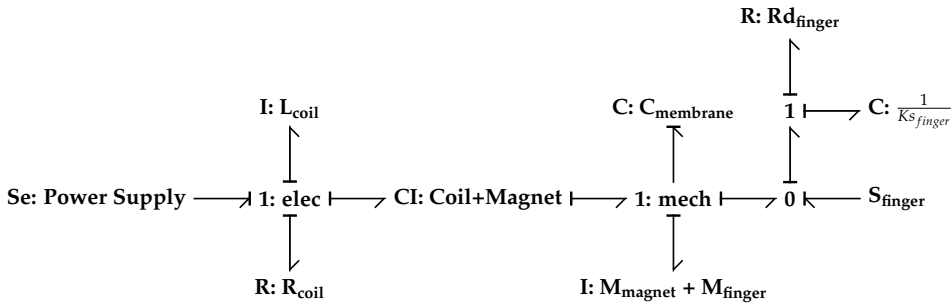


FIGURE 2.13: Bond graph of the coil-magnet-membrane system.

In the next subsections, we will analyze the physical laws that govern the behavior of the system and how to model them to create this bond graph.

2.4.1 Neodymium magnets (magnetic strength wrt class and dimensions)

Neodymium magnets are a type of rare-earth magnet, they are the strongest type of permanent magnets made commercially. They are made of an alloy of neodymium, iron, and boron and their strength depends on the percentage of neodymium in the alloy and on its crystalline structure. They are classified based on their maximum energy product, which is the maximum amount of energy that can be stored in a magnet. Modern neodymium magnets start from N35 and go up to N52 (even N55), the higher the number the stronger their magnetic field.

Considering a cylindrical magnet with a radius R_M and a thickness t we can calculate the magnetic field generated by it at a distance z from a pole surface using the formula [19]:

$$B_M(z) = \frac{B_r}{2} \left(\frac{t+z}{\sqrt{R_M^2 + (z+t)^2}} - \frac{z}{\sqrt{R_M^2 + z^2}} \right) \quad (2.30)$$

Where:

- B_r is the remanence of the magnet [T]
- R_M is the radius of the magnet [m]
- t is the thickness of the magnet [m]
- z is the distance from a pole surface of the magnet [m]

The remanence of a magnet is the magnetic field that remains in the magnet after the external magnetic field is removed and depends on the N grade of the magnet.

2.4.2 Magnetic force between magnet and coil

To calculate the magnetic repulsion force between the coil and a permanent magnet we consider them aligned with their centers coinciding on the z-axis.

The force between a magnet and a coil can be calculated using the magnetic field generated by the coil and magnet. Knowing their closed-form expression we can calculate the force using this formula:

$$F = \nabla(\vec{m}_M \cdot \vec{B}_C) \quad (2.31)$$

Goudsmit Grade	Remanence B_r [mT]	
	min value	typical value
N35	1170	1210
N38	1220	1260
N40	1260	1290
N42	1290	1320
N45	1320	1370
N48	1370	1420
N50	1400	1460
N52	1420	1470

TABLE 2.2: Magnetic field remanence of different N grade neodymium magnets.

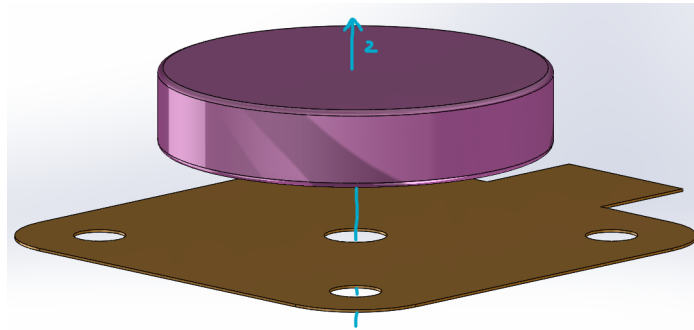


FIGURE 2.14: Coil and magnet position in space.

Where:

- \vec{m}_M is the magnetic moment of the magnet [A/m]
- \vec{B}_C is the magnetic field generated by the coil [T]

The magnetic momentum of the magnet is defined as:

$$\vec{m}_M = \left(0 \quad 0 \quad \frac{B_M(z)}{\mu} \right) \quad (2.32)$$

Where:

- $B_M(z)$ is the magnetic field generated by the permanent magnet [T]
- μ is the magnetic permeability of the medium [H/m]

We can calculate the magnetic field generated by the coil at a distance using equation 2.12 (considering our coil as two in parallel) and the magnetic field generated by a cylindrical magnet at a distance z using equation 2.30.

Doing the calculations, the resulting force in function of the distance z is given by:

$$F = \frac{B_r IN R_C^2 \left(\frac{1}{\sqrt{\sigma_1}} - \frac{1}{\sqrt{\sigma_2}} + \frac{z^2}{\sigma_2^{3/2}} - \frac{2(t+z)^2}{2\sigma_1^{3/2}} \right)}{2\sigma_3^{3/2}} + B_C(I) \cdot \frac{3z \left(\frac{z}{\sqrt{\sigma_2}} - \frac{t+z}{\sqrt{\sigma_1}} \right)}{2\sigma_3} \quad (2.33)$$

Where:

- N is the number of spires of a one-layer coil

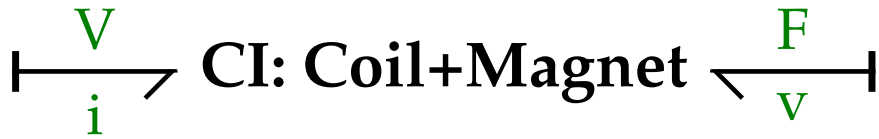


FIGURE 2.15: Coil-Magnet Transducer bond graph.

$$F(q, i) = \frac{1}{2} \frac{d(L(q) \cdot m_M(q))}{dq} i \quad (2.35)$$

$$\lambda = L(q)i \quad (2.36)$$

- I is the current flowing through the coil [A]
- B_C is the coil magnetic field calculated as in 2.12 [T]
- R_C is the coil average radius (r' in equation 2.12) [m]
- $\sigma_1 = R_M^2 + (t + z)^2$
- $\sigma_2 = R_M^2 + z^2$
- $\sigma_3 = R_C^2 + z^2$

So we can model the coil-magnet system as a **Transducer** element that converts the current flowing through the coil into a force acting on the magnet.

$$B_C(z, I) = \frac{\mu N I R_C^2}{2(R_C^2 + z^2)^{\frac{3}{2}}} \rightarrow B_C(q, i) = \frac{1}{2} L(q) i \quad (2.34)$$

2.4.3 Membrane-magnet system

The magnet needs to be suspended to allow it to move freely only on the z-axis, to achieve this we need a structure that constrains the lateral motion of the magnet and needs to also be able to vibrate freely with it. To do this we can use a flexible membrane that can deform under the magnetic field generated by the coil and the magnet.

As an example, we will analyze the membrane structure of the last type of prototype we implemented

This membrane is a simple Celtic-cross structure made of thin silicone integrated with the entire structure of the device, the membrane is built with a central cylindrical chamber used to trap the magnet in the center of the cross.

The membrane can be modeled as a mass-spring-damper system.

Membrane stiffness

The membrane stiffness can be calculated using Young's modulus of the material, the geometry of the membrane and the load characteristics.

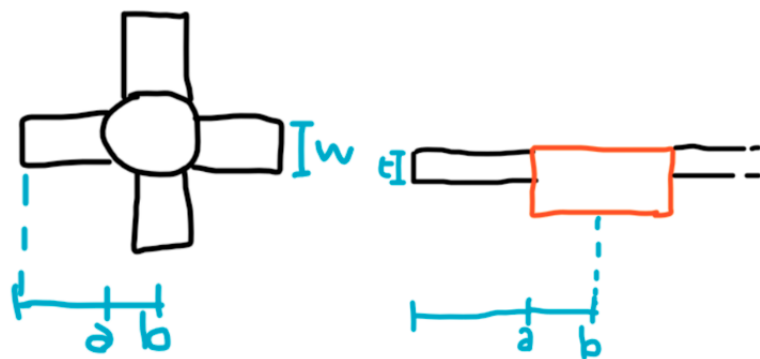


FIGURE 2.16: Membrane structure of the last prototype.

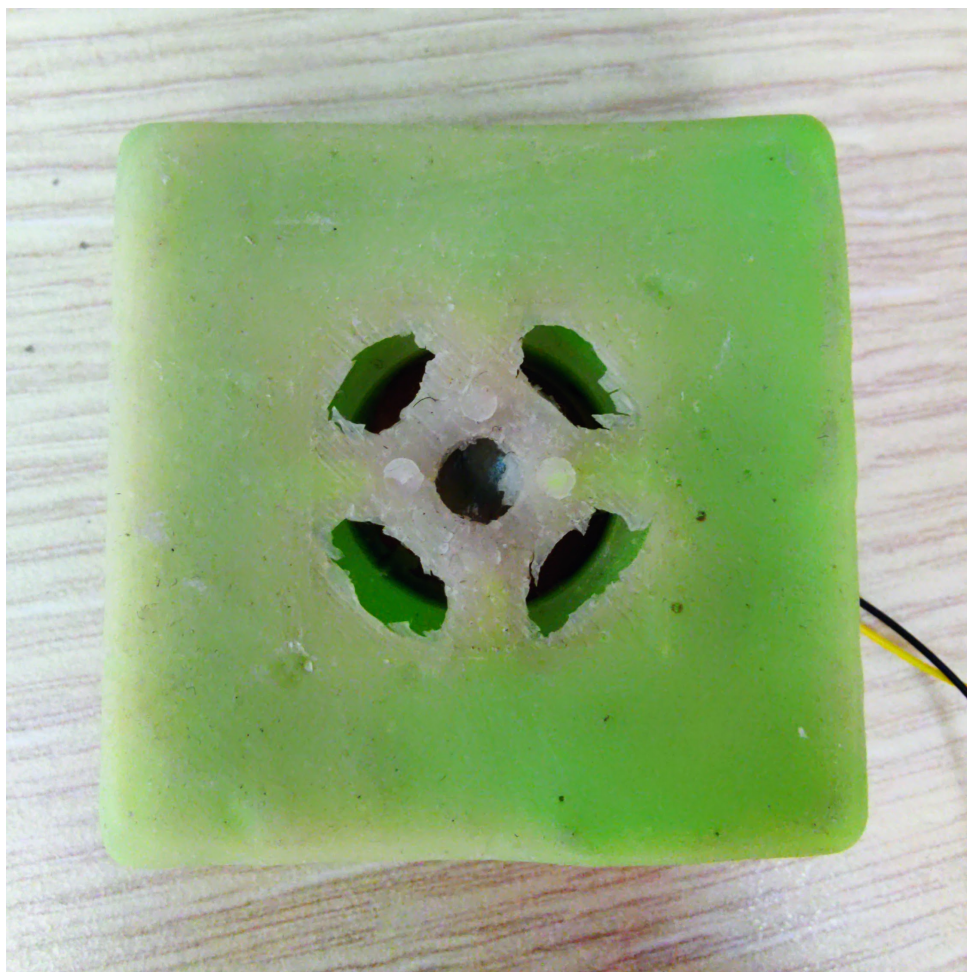


FIGURE 2.17: Membrane of the last prototype with the magnet trapped in the center.

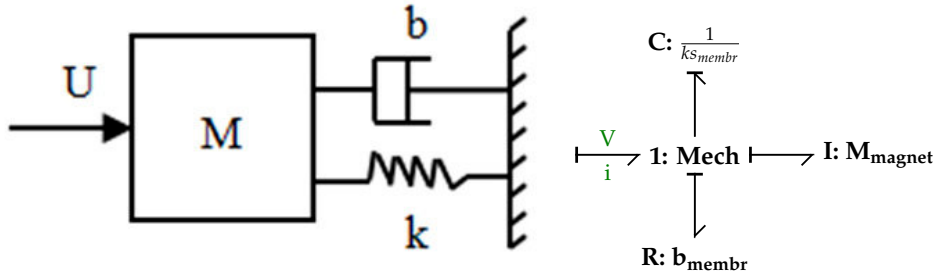


FIGURE 2.18: Bond graph of the membrane-magnet system.

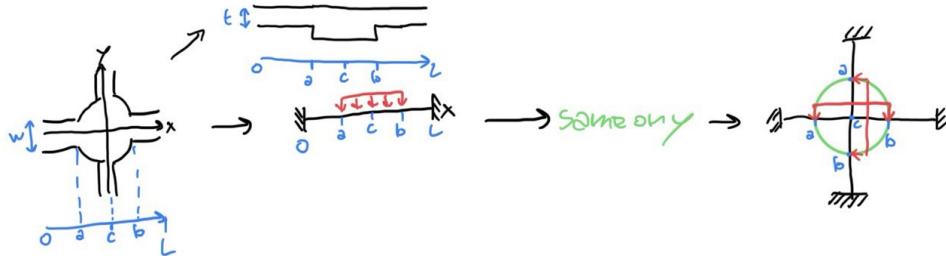


FIGURE 2.19: Membrane structure simplified as two fixed beams.

The geometry of the membrane can be modeled as two **fixed beams** perpendicular to each other and connected at the center. They are both under a shared **partially distributed load**, the magnet's weight.

Where we approximate the distribution of weight on the membrane as the weight of the magnet distributed across its diameter. For each beam, the distributed load can be calculated as:

$$w = \frac{\frac{M_{magnet}}{2} g}{2r} \quad (2.37)$$

Where:

- w is the distributed load [N/m]
- M_{magnet} is the mass of the magnet [N]
- g is the gravitational acceleration [m/s^2]
- r is the radius of the magnet [m]

We approximate by considering only half of the magnet's weight as we have two beams supporting the magnet.

Then the stiffness of a single beam is defined as:

$$ks = \frac{P}{\delta_{max}} \quad (2.38)$$

Where:

- ks is the stiffness of the beam [N/m]
- P is the load on the beam [N]
- δ_{max} is the deflection of the beam [m]

Considering the structure shown in figure 2.19, the maximum deflection of a fixed beam under a distributed load can be calculated as:

$$\delta_{max} = -\frac{R_A c^3}{6EI} - \frac{M_A c^2}{2EI} + \frac{w(c-a)^4}{24EI} \quad (2.39)$$

Where:

- δ is the deflection of the beam [m]
- R_A is the reaction force at the origin of the beam [N]
- M_A is the moment at the origin of the beam [Nm]
- E is the Young's modulus of the material [Pa]
- I is the second moment of inertia of the beam [m^4]
- w is the distributed load [N/m]
- c is the distance between the origin of the beam and its center [m]
- a is the distance between the origin of the beam and the start of the distributed load [m]

We will only focus on the calculation of the second moment of inertia of the beam, the equations for the other parameters can be found in the reference [10].

The beam can be simplified as a parallelepiped with a rectangular section, and the second moment of inertia on x can be calculated as:

$$I_x = \frac{wt^3}{12} \quad (2.40)$$

Where:

- I_x is the second moment of inertia on the x-axis [m^4]
- w is the width of one membrane arm as in figure 2.19[m]
- t is the thickness of the membrane as in figure 2.19[m]

Then we can consider the 2 beams as 2 springs in parallel, the total stiffness of the membrane can be calculated as:

$$ks_{membr} = 2ks \quad (2.41)$$

Membrane damping

The damping for a cantilever beam is neglectable, so we can remove the resistive component from the mechanical model.

2.4.4 Finger grasping model

At last, we have also to model the finger grasping the device, we can derive the model from the one used in [8] for the human finger.

This model describes two fingers grasping an object, for our case, we can simplify it to a single finger grasping the device. Also, we can neglect the friction between the

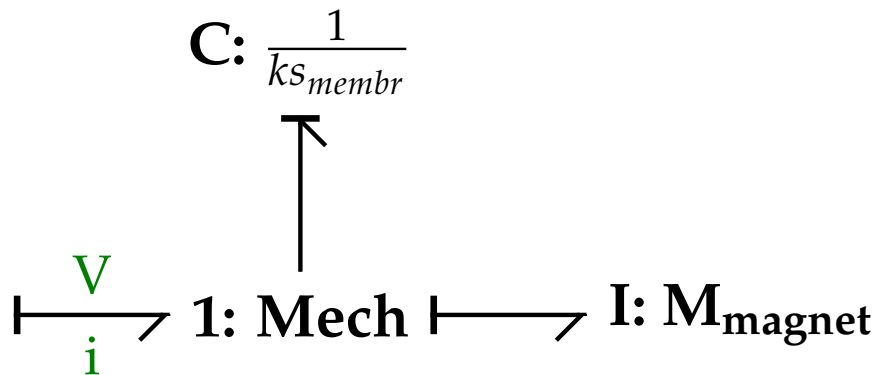


FIGURE 2.20: Final mechanical bond-graph of the membrane and magnet.

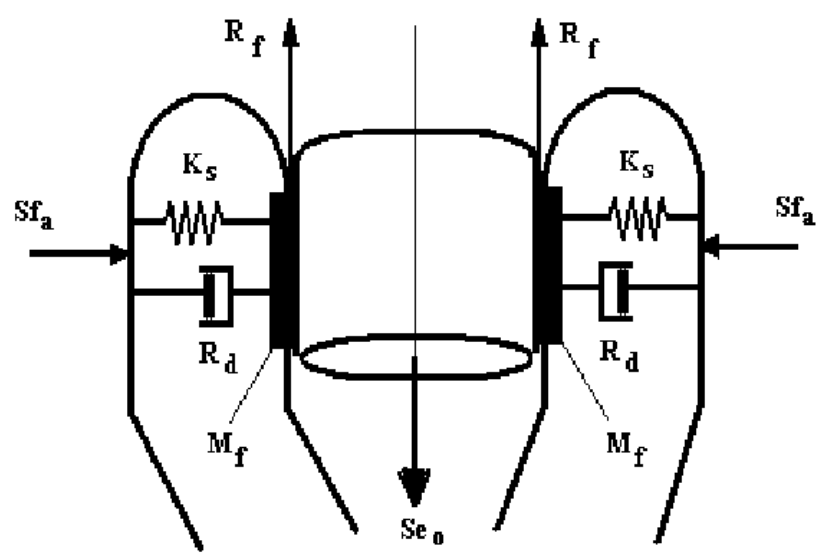


FIGURE 2.21: Model of two soft fingers grasping the object.

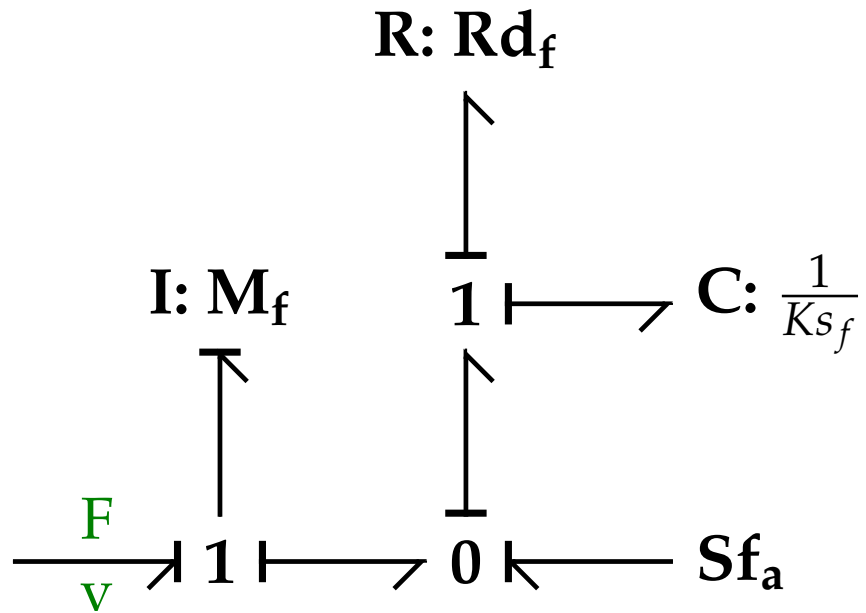


FIGURE 2.22: Bond graph of the finger grasping model.

finger and the device as the device will be tested positioned on a flat surface with only the finger touching it from above.

Chapter 3

Overview of Haptic Feedback

Computer Haptic Feedback or Haptics, in short, is the research field that deals with the need to be able to digitalize the human sense of touch and reproduce it. Despite the research done in this field since the mid-20th century, the technology is still in its infancy. The main reason for this is the complexity of the human sense of touch which we still don't understand fully. This, in turn, doesn't allow us to even approximately match the capabilities of the human sense of touch; but we can still use this infant technology to reproduce simple sensations. This sensation can be used in many fields, from the entertainment industry to the medical field, from the military to the automotive industry to convey information that we do not normally acquire via touch, such as notifications and warnings related to particular events, guidance instructions, and even crude reproduction of textures. In this chapter, we will give an overview of the human sense of touch and the state of art technologies used to reproduce it.

3.1 Physics of Haptic Feedback

3.1.1 Biology of Haptic Sensing

The human tactile sensing system can measure specific properties of materials, such as temperature, texture, shape, force, fine-form features, mass distribution, friction, hardness and viscoelasticity, through physical contact between the human skin and the object. Even the changing state of the interaction, such as gravitational and inertial effects, can be perceived through the sense of touch. As the sensing system works through the skin, it doesn't rely on a localized sensory organ but behaves as a distributed system, also different parts of the body have different thresholds of sensitivity. For these reasons, it's difficult to treat a tactile signal as a well-defined quantity like visual and audio signals and its complex nature makes it difficult to replicate its functioning in science or engineering tasks.

The sense of touch is based on the somatosensory system, which is a complex system of nerve endings and touch receptors in the skin. The somatosensory system is composed of four main types of receptors:

- **Mechanoreceptors** - These are the most common type of tactile receptors in the skin. They are responsible for sensing pressure, vibration, stretching, and brushing.
- **Thermoreceptors** - These receptors are responsible for sensing temperature changes in the skin. There are two main types of thermoreceptors: warm receptors and cold receptors.

- **Nociceptors** - These receptors are responsible for sensing pain and tissue damage. They are activated by noxious stimuli, such as extreme temperatures, pressure, or chemicals.
- **Proprioceptors** - These receptors are responsible for sensing the position and movement of the body. They are located in the muscles, tendons, and joints, and provide feedback to the brain about the relative position between different parts of the body.

The most important receptors for haptic feedback are the mechanoreceptors, they react to mechanical stimuli by producing signals in the form of streams of voltage pulses at high frequencies, the stronger the stimulus higher the frequency of the pulses. When the cell adapts to the stimulus, the pulse frequency subsides to its normal rate. Considering the goal of this research we can focus on the mechanoreceptors that are responsible for sensing pressure and vibration, these are the Pacinian corpuscles and the Meissner corpuscles. The first ones are more sensible to high-frequency vibrations (200-550Hz), while the second ones are more for low-frequency vibrations (20-40Hz). [3]

3.1.2 Haptic sensitivity

As the mechanoreceptors are enveloped in various skin layers, their sensitivity to vibrations will not be infinite. The strength of the sensation will depend on the frequency and amplitude of the vibration. The amplitude of the vibration can be considered in terms of the acceleration of the membrane-magnet system. Previous works [14] found that, for a pulp contact area ranging from 53 to 176.7 mm², the threshold of detection of vibrations was between 0.1778 and 0.5623 m/s² (in the work specified as 105-115 dB (re 1e-6m/s²) for sinusoidal stimuli ranging from 100 to 250 Hz.

+ For frequencies close to 125Hz the threshold should also lower as the finger pulp reaches its resonance frequency [21].

The study also highlights that the sensitivity depends on the constant pressure force applied on the skin in conjunction with the vibration. They found that under active pressing force, the sensitivity threshold decreases to 0.027-0.143 m/s² (in the work specified as 68.5-83.1 dB (re 1e-6m/s²) for a constant applied force of 1.6N.

For higher pressure forces the sensitivity threshold decreases even further Fig. 3.1.

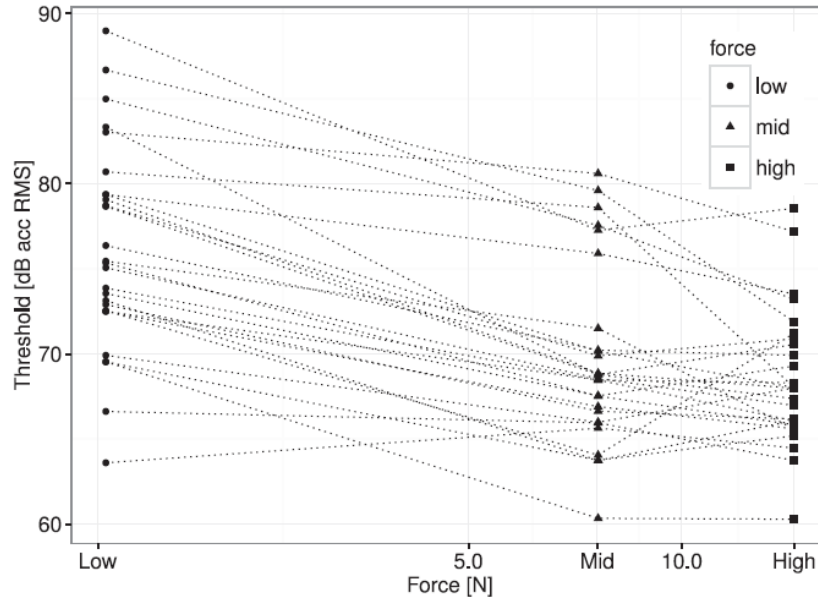


FIGURE 3.1: Vibrotactile Sensitivity as a function of the applied pressure force.

3.2 State of the Art in vibrotactile haptic feedback

For now, state of the art in haptic feedback is still in its infancy. The main reason for this is the complexity of the human sense of touch which we still don't understand fully. The best technology we have for now to reproduce haptic feedback through vibrotactile means is the piezoelectric actuator.

3.2.1 Piezoelectric actuators

Piezoelectric actuators are a very interesting technology based on the piezoelectric effect. Materials exhibiting this effect, such as certain ceramics and crystals, possess the ability to convert electrical energy into mechanical motion, and vice versa.

The operating principle of piezoelectric actuators relies on the application of an electric field across the piezoelectric material. This electric field induces a deformation within the material, causing it to expand or contract depending on the polarity of the applied voltage. This minute deformation translates into highly precise mechanical displacement, enabling piezoelectric actuators to achieve nanometer-scale resolutions with remarkable speed and accuracy.

One of the defining characteristics of piezoelectric actuators is their rapid response time. Unlike traditional electromagnetic actuators, which may suffer from inertia and mechanical backlash, piezoelectric actuators can swiftly change their state in response to electrical signals.

Frequency response

Piezoelectric actuators are perfect for haptic applications as they can provide a wide range of frequencies. Piezo specifically engineered for haptic feedback can provide a frequency range from 1 Hz to 1 kHz.

All piezoelectric actuators have a natural frequency at which they resonate. This frequency is determined by the mechanical properties of the actuator, such as its mass and stiffness, as well as the electrical properties of the piezoelectric material. The important thing to note is that this frequency also depends on the load that the actuator is driving:

$$f_{res} = \frac{1}{2\pi} \sqrt{\frac{k}{m_{eff} + m_{load}}} \quad (3.1)$$

Where:

- f_{res} = Resonant frequency [Hz]
- k = Stiffness of the piezo actuator [N/m]
- m_{eff} = Effective mass of the actuator [kg]
- m_{load} = Mass of the load [kg]

As the frequency of the actuator approaches its resonant frequency, the amplitude of the actuator's motion increases significantly. This phenomenon must be taken into account when designing a control system for the piezo actuator, as at maximum voltage the actuator could be damaged if in resonance.

Force performances

Taking as an example a piezo actuator built specifically for haptic feedback, the PowerHap series from TDK [15], we can see that the actuator can provide a force up to 20N in a frequency range from 1 Hz to 500Hz.

Power consumption

Considering still as an example the PowerHap series from TDK, we can read from the datasheet that the actuator can be run with a peak voltage of 120V and an average current of 0.432A (calculated using [16] in the case of a square wave signal of 500Hz). This means that the actuator can consume up to 25.9W of power at its peak frequency. In the same condition, it will also dissipate about 2.59W of power as heat.

3.2.2 Texture rendering

- frequency requirements
- force requirements
- response time

Chapter 4

Powering circuit design

In this chapter, we will present some of the engineering challenges faced during the design of a power circuit for our flexible voice coil actuator. We will mostly describe an ideal circuit as we will later demonstrate that running this actuator would require very advanced analog circuitry, comprised of high-cost components. Most of the tests we will present have been done using a bench signal generator and amplifier.

4.1 Power Circuit Block diagram

To design the power circuit for the flexible voice coil actuator, we started by analyzing the requirements of the actuator. First of all, we want the coil to be driven with a sinusoidal AC signal at various frequencies and amplitudes; so the first component to consider it's the system's controller which in this case, can be a simple signal generator. For our application, we chose a simple ESP32 microcontroller, which has an integrated DAC.

Then we have to consider the power requirements to run the chosen coil. The impedance of a Flexar coil, as we discussed before, is in the order of 30Ω . The impedance of the coil is too low to be driven directly by the ESP32 DAC, so a power stage is needed. For the sake of simplicity, we chose to implement a power stage with a fixed gain of 10.

Then we want the amplitude of the signal to be adjustable, so we need a conditioning circuit to adjust the amplitude of the signal coming from the DAC before being amplified.

The control circuit can be summarized as a block diagram, as shown in figure 4.1.



FIGURE 4.1: Block diagram of the power circuit.

4.2 Controller

The controller in this application has to be a signal generator that can produce a waveform that can be amplified and sent to the coil. The controller we used for

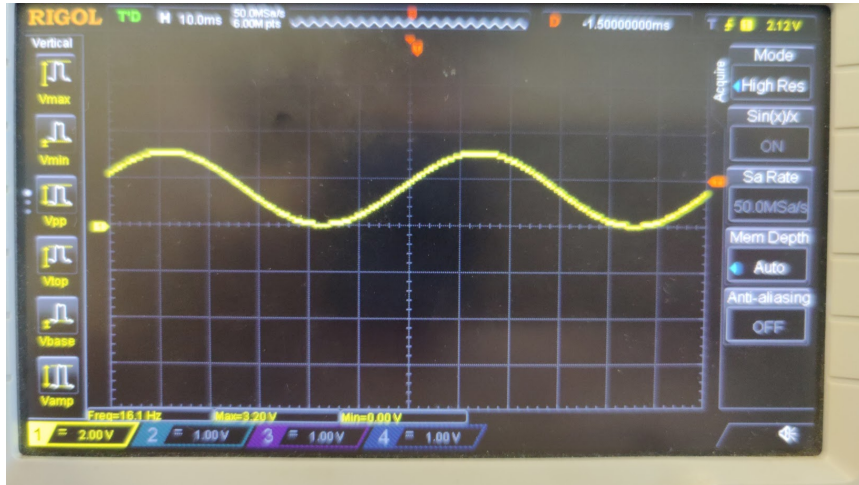


FIGURE 4.2: ESP32 16Hz Sine wave generated by the ESP32 Signal Generator software.

testing is an ESP32 microcontroller. We chose this controller as the first test hardware for its simplicity of programming and its integrated DAC.

4.2.1 ESP32 DAC Characteristics

The DAC included in the ESP32 is a pretty basic one but as a first test, it is enough. The DAC has a resolution of 8 bits, and it can output a voltage between 0 and 3.3V with a maximum current output of 12mA.

4.2.2 ESP32 waveform generator

Using a simple program the ESP32 can be used as a pretty capable waveform generator. The software we used is the **ESP32 Signal Generator** from corz.org [2]. This software allows the user to generate the following waveforms:

- Sine wave from 16Hz to 500kHz
- Square wave from 1Hz to 40MHz
- Triangle wave from 153Hz to 150kHz
- Sawtooth wave from 153Hz to 150kHz

Between these ranges of frequencies, the generated waveforms are pretty accurate.

4.3 Signal Conditioning Circuit

We know that the controller DAC outputs a voltage between 0 and 3.3V, the power stage has a gain of 10, and that to drive Flexar's coils, at their rated maximum power of 0.8W, we need to provide a voltage of about 6V at a current of 0.2A.

A very simple solution is to implement a variable voltage divider to adjust the amplitude of the signal coming from the DAC. We chose a maximum dividing factor of 10 to match the power stage gain.

Where:

- V_{DAC} is the voltage coming from the controller DAC [0,3.3]V.

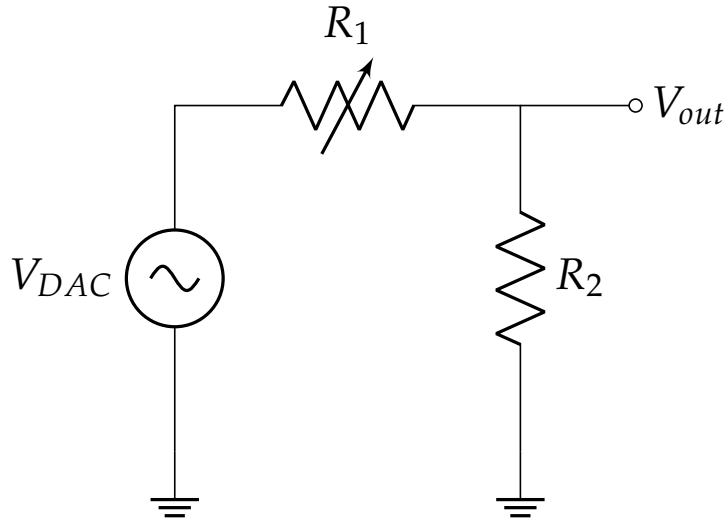


FIGURE 4.3: Signal conditioning circuit.

- R_1 is a $100k\Omega$ potentiometer to adjust the amplitude of the signal.
- R_2 is a $10k\Omega$ resistor to set the maximum amplitude of the signal.
- V_{out} is the output voltage of the conditioning circuit [0, 0.33]V.

The output voltage of the conditioning circuit is given by the following formula:

$$V_{out} = V_{DAC} \cdot \frac{R_1}{R_1 + R_2} \quad (4.1)$$

The values of R_1 and R_2 have been chosen to be $100k\Omega$ and $10k\Omega$ respectively, as they are standard values, provide a good range of adjustment for the amplitude of the signal, and their order is big enough to work with the provided DAC current of 12mA.

4.4 Amplifier circuit

As the Flexar's coil impedance is 30Ω , and the maximum power they can withstand is 0.8W, the power stage must be able to provide a voltage of about **6V** at a current of **0.2A**.

Such a high current requires the use of a power amplifier, usually an off-the-shelf audio amplifier could be used but such devices are built to handle only the audible frequency range (20Hz-20kHz), and our actuators must be able to work between 1Hz and 1kHz which corresponds to the human tactile perception range.

A solution is to implement a custom amplifying circuit based on a special type of operational amplifier, the Power OP-AMP.

4.4.1 Power Operational Amplifiers

Power operational amplifiers (power op-amps) are a specialized class of operational amplifiers designed to handle higher current and power levels than standard op-amps. While traditional op-amps are primarily used for signal processing and conditioning in low-power applications, power op-amps are essential for driving heavy

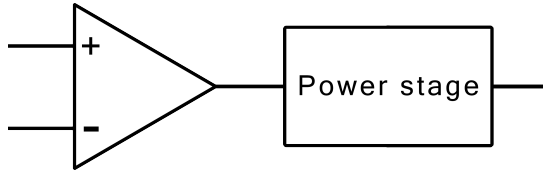


FIGURE 4.4: Power Op Amp block diagram.

loads, including motors, speakers, and other devices that require substantial power. Power op-amps integrate the fundamental principles of conventional op-amps—such as high gain, high input impedance, and low output impedance—with the ability to deliver higher current and power.

These devices are composed of simple op-amp circuits with a power stage, usually a power transistor, connected to the output of the op-amp. The power stage is responsible for delivering the required current to the load, while the op-amp provides the necessary voltage gain and feedback control.

Power op-amp characteristics

Any op-amp that can deliver more than 100mA of current is considered a power op-amp; there exist models that can deliver up to 10A. For our application, we chose a power op-amp that can deliver up to 1A of current, as it is more than enough to drive the Flexar's coils for simple AC signals. Another factor for this decision is the high cost of these components, especially at higher current ratings, due to their complexity and the scarcity of requests for this type of component from the market.

The component we landed on is the **L272** from STMicroelectronics, this small chip can deliver up to a sustained 1A of current, 1.5A of peak current, and can handle a maximum supply voltage of 28V.

In dynamic conditions is also to be noted that the L272 has a slew rate of $1\frac{V}{\mu s}$ and, a gain-bandwidth product of 350kHz [9].

Power dissipation problems

A big problem with power op-amps is the power dissipation, as they are designed to deliver high current levels, they also dissipate a lot of power, which can lead to overheating and damage to the device.

For example, the L272 can handle up to 145°C but at only 5W it reaches 75°C, so a heat sink is required to keep the device at a safe temperature.

4.4.2 High Power Voltage Amplifier

As we specified before we decided to implement a power stage with a gain of 10, starting with the circuit of a simple inverting amplifier (the real gain is -10 but for the sake of our application a wave flipped by 180° is acceptable).

The gain can be calculated using the following formula:

$$A = \frac{V_{out}}{V_{in}} = -\frac{R_f}{R_1} \quad (4.2)$$

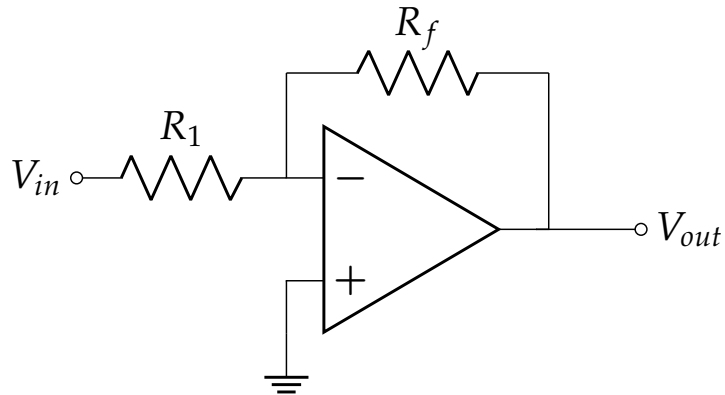


FIGURE 4.5: Inverting amplifier circuit.

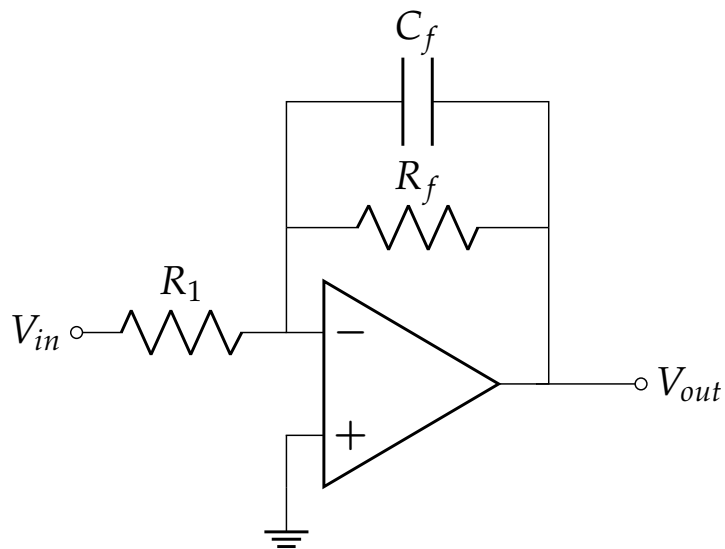


FIGURE 4.6: Inverting amplifier circuit with low-pass filter.

Where:

- V_{in} is the input voltage.
- V_{out} is the output voltage.
- R_1 is the input resistor.
- R_f is the feedback resistor.

The values of R_1 and R_f have been chosen to be $4.7k\Omega$ and $47k\Omega$ respectively, as they are standard values and their order is big enough to work with the provided DAC current of $12mA$.

4.4.3 Noise filtering

While implementing the amplifier circuit, we noticed that the output signal had a lot of high-frequency noise, which was not present in the input signal.

To solve this problem, we decided to implement a simple low-pass filter adding a capacitor in parallel with the feedback resistor.

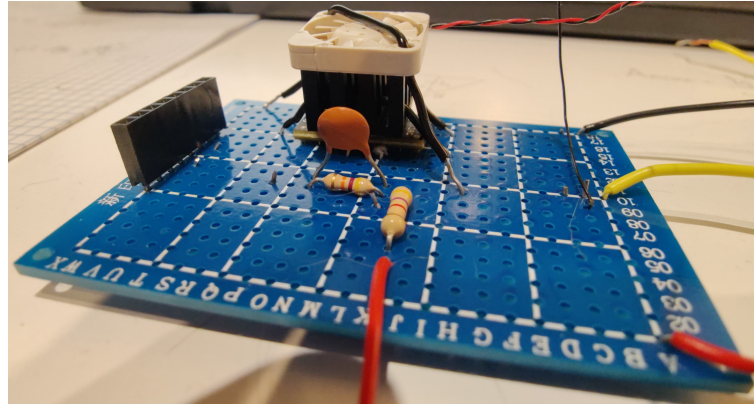


FIGURE 4.7: Picture of the implemented power stage.

The cutoff frequency of the filter can be calculated using the following formula:

$$f_c = \frac{1}{2\pi R_f C_f} \quad (4.3)$$

Where:

- f_c is the cutoff frequency.
- R_f is the feedback resistor.
- C_f is the capacitor in parallel with the feedback resistor.

We set a cutoff frequency of 50kHz, as it is high enough to filter out the noise but low enough to keep the signal intact. To achieve this, we chose a capacitor of 680pF, as it is a standard value and provides a cutoff frequency of 50kHz with the chosen feedback resistor.

Chapter 5

Implementation and Prototypes

5.1 Coils alternatives

This research was originally born from the willingness to explore the possibility of exploiting the technology of flexible coil inductors by using one produced by the research group Helmholtz-Zentrum Dresden-Rossendorf (HZDR) in Dresden, Germany [5]. After testing this coil, we realized its limitations and decided to explore other alternatives. For our research, we landed on Flexar coils, which as we discussed before are flexible PCB coils produced by the company **microbots** [11]. In this section, we will compare the Dresden coil with the Flexar coil, which is the one we chose to use in our research.

5.1.1 Dresda coils

The technology the HZDR team used to produce their coil is based on circuit inkjet printing. Circuit inkjet printing consists of using a printer to deposit conductive ink on a substrate. In this application, they used a flexible substrate to print the coil to allow it to be bent. After printing the conductive ink is tinned to improve the conductivity of the coil and allow it to be soldered to other components.

Low resistance and high power needs

The Dresden coils have a **resistance** of about 2Ω , **external radius** of $5\text{e-}3\text{m}$, **internal one** of $0.84\text{e-}3\text{m}$, and **number of spires** equal to **11**. We also know from the HZDR test that the coil can handle up to about **500mA** before starting to release too much heat. This means a power limit of about **0.5W** for the coil.

The current limit is due to the very low resistance of the coil as due to this limitation, for low applied voltages the coil will produce a lot of heat due to the Joule effect 2.3.2.

As we can see in figure 5.2, after 1V the power limit is already reached.

Low magnetic field strength

For the same reason as the power limit, the magnetic field produced by the Dresden coil is very low. Using the equation 2.11 we can calculate the magnetic field produced by the Dresden coil on its surface and plot it as a function of the voltage applied to the coil.



FIGURE 5.1: Dresden coil [5]

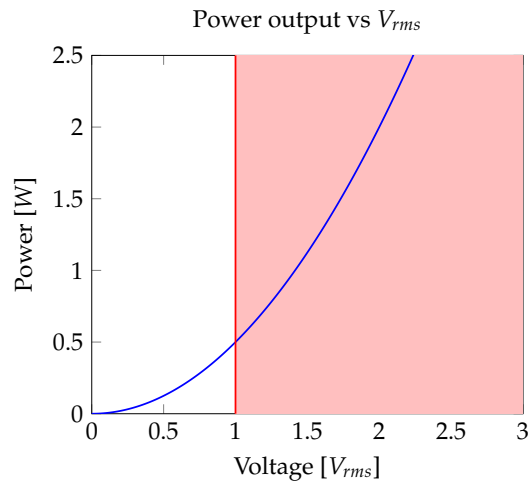


FIGURE 5.2: Power profile of the Dresden coil

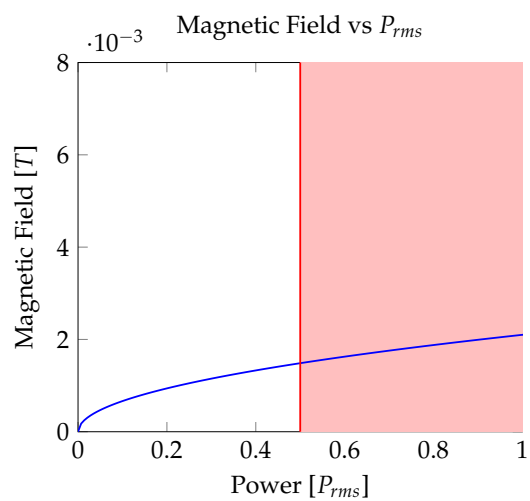


FIGURE 5.3: Magnetic field produced by the Dresden coil



FIGURE 5.4: Flexar coil

As we can see in figure 5.3, even at the power limit, the magnetic field produced by the Dresden coil is very low (in the order of 1mT).

Fragility and low flexibility

The Dresden coil is produced by using three layers of different materials. The first layer is the substrate, which is made of a material similar to paper, the second layer is the conductive ink, and the third layer is the tinning. The substrate is not very flexible, and neither is the tinning; this makes the spires of the coil easily damageable if bent repeatedly. Also, the tinning gets cracked by repeatedly heating and cooling the coil, which constantly happens during the coil's use. The tinning cracking would happen multiple times during our tests, and we would have to re-tin the damaged parts of the coil to keep using it.

5.1.2 Flexar coils

Flexar coils are flexible PCB coils designed by the independent researcher Carl Bugeja [1]. He designed these very thin flexible coils intending to use them to actuate very small robots and lightweight objects. This characteristic comes at the cost of not being able to produce very high magnetic fields. We will be using for this research an old model of the Flexar coil that precedes the opening of the company **microbots** [11].

Lower resistance and power needs

We previously discussed the Flexar coil's characteristics in section 2.3.2. But to sum up they have a **resistance** of about 30Ω , **external radius** of $6.86\text{e-}3\text{m}$, **internal one**

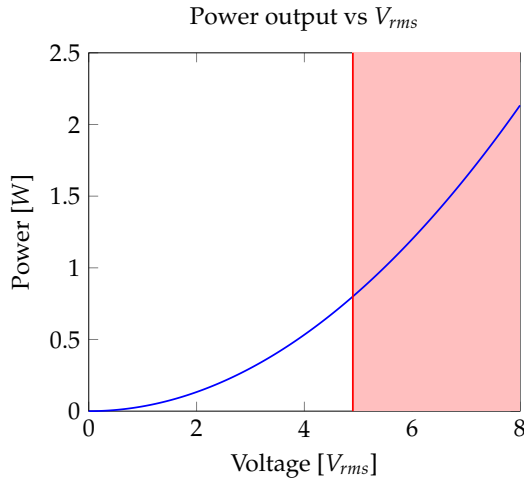


FIGURE 5.5: Power profile of the Flexar coil

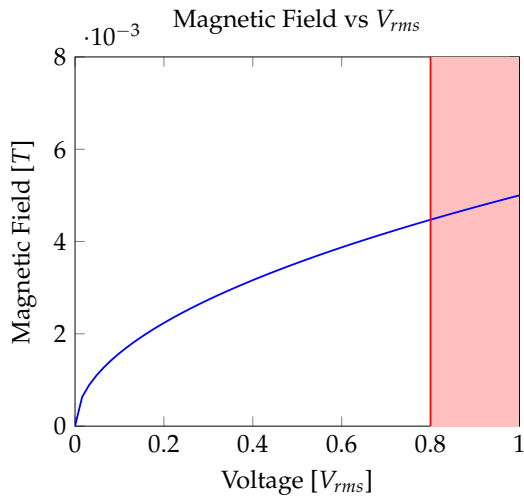


FIGURE 5.6: Magnetic field produced by the Flexar coil

of about **1e-4m**, and **number of spires** equal to **70** (composed of two coils of 35 in series). It can handle up to about **0.8W** before starting to release too much heat.

We report here the same graph as the previously cited section:

As we can see in figure 5.5, the Flexar coil can handle more power than the Dresden coil.

Higher magnetic field strength

Due to their characteristics, Flexar coils can produce higher magnetic fields than the Dresden coil but not unlike them, they are still limited by the power they can handle. As we can observe in figure 5.6, the Flexar coil, at the power limit of the Dresden coil, can produce a higher magnetic field (in the order of 2.5mT). This proves that the Flexar coil is more capable than the Dresden coil in producing magnetic fields but even at its power limit the field produced is still feeble (it is in the order of (4mT)).

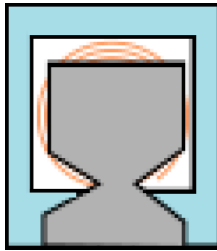


FIGURE 5.7: Dresden coil HZDR test setup

Higher flexibility

Flexible PCBs are made of a substrate of polyimide, which is a very flexible material. It can withstand being bent at a very tight radius multiple times without breaking.

Between the layers of polyimide, we have the copper traces that don't require any tinning to work. This makes the Flexar coil more durable than the Dresden coil, as it doesn't have any parts that can crack due to bending or heating and cooling.

Also, we observed that the Flexar coil can withstand temperatures in exceed of 100°C.

5.2 Rigid Prototypes

The goal of this research is to develop a flexible device but before delving into flexible prototypes we started by designing some rigid prototypes. The rigid prototypes were designed to test the concept of the device and to understand the limitations of the technology.

5.2.1 1st version - Dresden Coils testbed

The first prototype was designed to test the capabilities of the Dresden coils. In the previous research done by the HZDR team [5] they tested the coil using a simple piece of flexible magnetic tape as a membrane.

Flexible magnetic membrane

This membrane is shaped like a "fish" so the tail can be fixed on a plane and the head can be free to bend up and down.

When the coil was powered, the magnetic field produced by the coil would repel the membrane and bend it up. The coil would be powered with an AC signal at various frequencies, then one would need to keep his pulp suspended at a certain distance over the membrane and feel the vibration produced by the membrane. The pulp needed to be suspended at a certain distance to avoid pressing on the membrane, this would have caused the membrane to stop vibrating.

Adjustable height platform for coil and membrane

The most important thing to solve was to find a way to keep the pulp at a certain distance from the membrane. Firstly we designed a platform that could keep the finger steady.

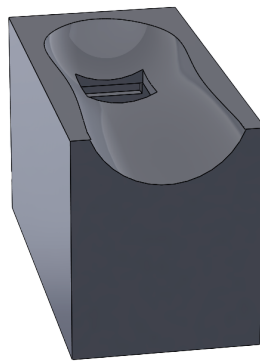


FIGURE 5.8: Finger platform

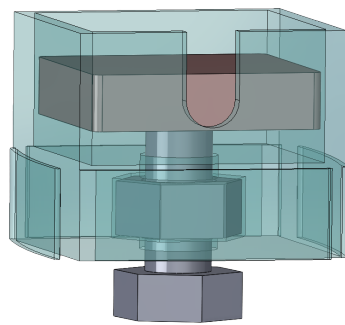


FIGURE 5.9: Adjustable platform

This platform was modeled to have an ergonomic cavity for the finger to rest in and a hole for the pulp to be suspended over the membrane. The square hole is large enough to allow the "fish" membrane to move freely. Under the hole, there is a large cavity where a mechanism is placed. This mechanism is a platform where the coil and membrane can be placed in a configuration similar to the one used in the HZDR experiment. The platform can then be raised or lowered to find the right distance between the membrane and the finger pulp. The mechanism is a simple screw that can be turned to raise or lower the platform.

Prototype usability

This prototype proved to be pretty finicky to use. The main problem was that distance couldn't be easily adjusted as the platform wouldn't remain stable enough on the screw. This meant that finding an optimal distance between the pulp and the membrane was difficult, especially because different people have different pulp thicknesses. Even if a distance that was good for one person was found, the vibration produced by the membrane was very weak and could barely be felt.

5.2.2 Wearable Rigid Prototypes

With this prototype, we wanted to try fixing most of the problems encountered with the previous prototype. Firstly we decided to substitute the Dresden coil with the Flexar one as it was more powerful. Then we wanted to decouple the membrane from the coil to prevent the membrane from being pressed by the pulp and remove

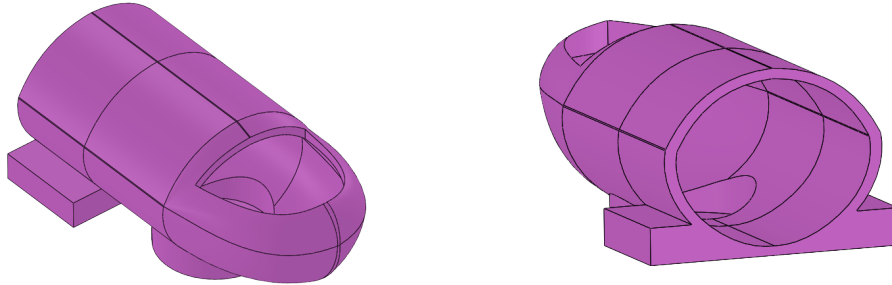


FIGURE 5.10: Finger silicon sleeve front and back view

the need for an adjustable platform to keep the coil at the right distance. Finally, we wanted to make the device wearable.

Finger-Membrane interface

After some testing, we found that a good way to decouple the membrane from the coil and better the transmission of vibrations to the finger was to use a small high-performance magnet attached directly to the finger pulp.

For our testing, we used an N42-grade neodymium cylindrical magnet with a diameter of **10mm** and a height of **3mm**. This magnet was fixed to the index pulp of the tester using some non-toxic glue and then he would be able to feel substantial vibrations by moving his pulp closer to the powered-on coil (with an AC signal).

Considering this knowledge, we designed a silicon sleeve that could be worn on the finger, this sleeve has a cavity for the magnet to be inserted into and be kept near the skin.

This silicon sleeve was designed to be scalable for different finger sizes and to be easily worn and removed. The part was produced by silicon casting inside a two-part 3D printed mold.

The design is composed of three parts:

- **Silicon sleeve:** This part was modeled by us on the profile of a real 3d scanned index finger, it can be automatically scaled by specifying the index's width as all the measurements are based on that value.
- **Magnet hole:** The hole is designed based on the diameter of the magnet and its height. We also had to find the right height tolerance between the magnet and the pulp to avoid that it could press on the finger too much, impeding vibrations.
- **Mounting wings:** On the sides of the sleeve we have two parallelepipedal wings that are used to mount the sleeve to the structure where the coil will be attached (described in the following section).

Another design problem to solve was the positioning of the magnet, as the design had the goal of being adaptable to different fingertip sizes, we had to consider multiple finger widths. For the magnet position we chose the center to be placed on the symmetry axis of the pulp, then we based the design on index fingers with widths between **13mm** and **20mm** [6]. That meant that for 13mm fingers, the magnet size (10mm) was barely smaller than the finger's width, so knowing that the finger tends

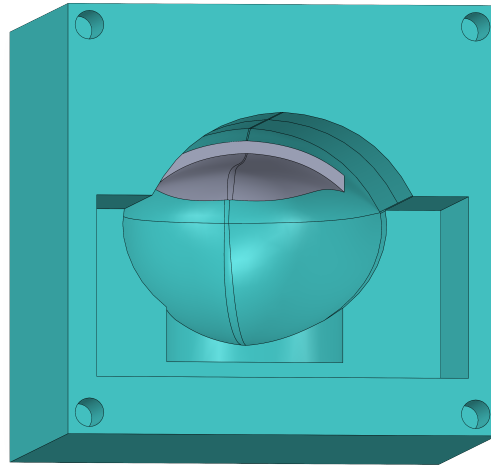


FIGURE 5.11: Mold cavity

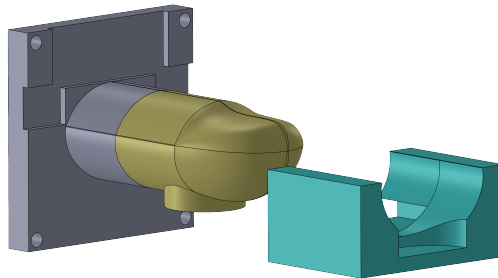


FIGURE 5.12: Mold core

to get even narrower toward the tip, we had to place the magnet center closer to the first interphalangeal fold rather than to the pulp's center.

Sleeve production

The sleeve was produced by silicon casting inside a two-part 3D printed mold:

- **Mold cavity:** The cavity was designed based on the 3D model of an index finger, with the addition of a small surface to produce the opening for the fingernail (the part in grey in figure 5.11) and half of the hole necessary to create the magnet cavity.
- **Mold core:** The core was designed to be the negative of the cavity, including a part to create the other half of the magnet cavity and mounting wings (the part in light blue in figure 5.12). The negative is scaled down a bit to create a casting clearance of about 0.8mm. This part also includes a cap that is screwed on the cavity to keep the core suspended in the silicon.

The part went through multiple iterations to land on the right thicknesses for the sleeve itself, it needed to be thin enough to be adaptable to multiple fingers (considering similar widths) but not so thin as to be durable enough.

The material used for the casting was a two-component silicon rubber from ResChimica. We tested two different types of silicon, one with a shore hardness of 12 [17] and one with a shore hardness of 35 [18].

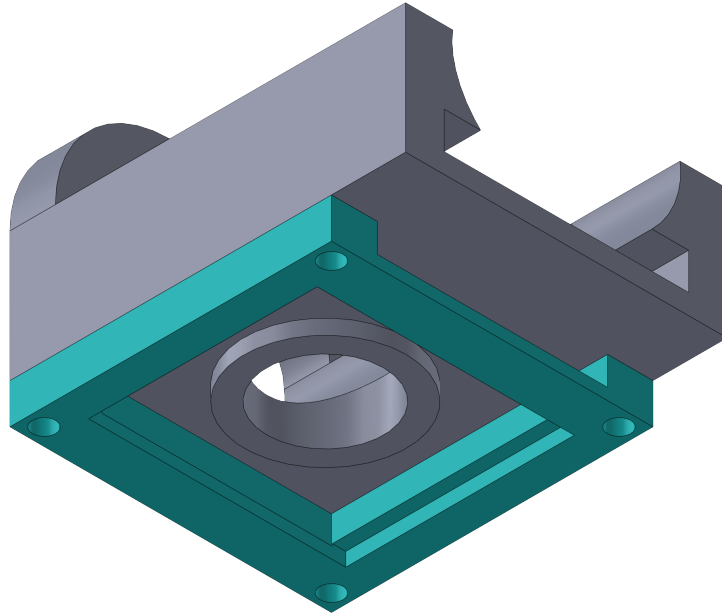


FIGURE 5.13: Explode of the complete silicon finger sleeve holder

From our tests, we found that the silicon with a shore hardness of 35 was too rigid and absorbed too much vibration so we decided to use the softer one. The only problem with this softer silicon was its minimum curing time of 3 hours at room temperature which always had to be increased as it never cured completely in that time.

Keep the distance from the coil

We then focused on a structure able to keep the coil at a fixed distance from the silicon sleeve and magnet. The design goals for this device were that it should be lightweight, easily wearable and adaptable to multiple sleeves' sizes.

After multiple iterations, we landed on a three-component design.

- **Sleeve holder:** This component is the structure where the sleeve can be attached, this is done by inserting the mounting wings inside the two squared holes on the bottom of the part. The circle hole at the center of the component is where the magnet cavity of the sleeve with the magnet inside will be placed. The arch on the component front is present to allow the tip of the finger to support the weight of the structure.
- **Coil trap:** This component is the structure where the coil is inserted. This component is composed of 3 parts, a heatsink, a coil holder and a mask to screw the heatsink to the sleeve holder. The coil is sandwiched between the heatsink (the part in bronze) and the coil holder (the part in grey). Then they are screwed together to the sleeve holder.

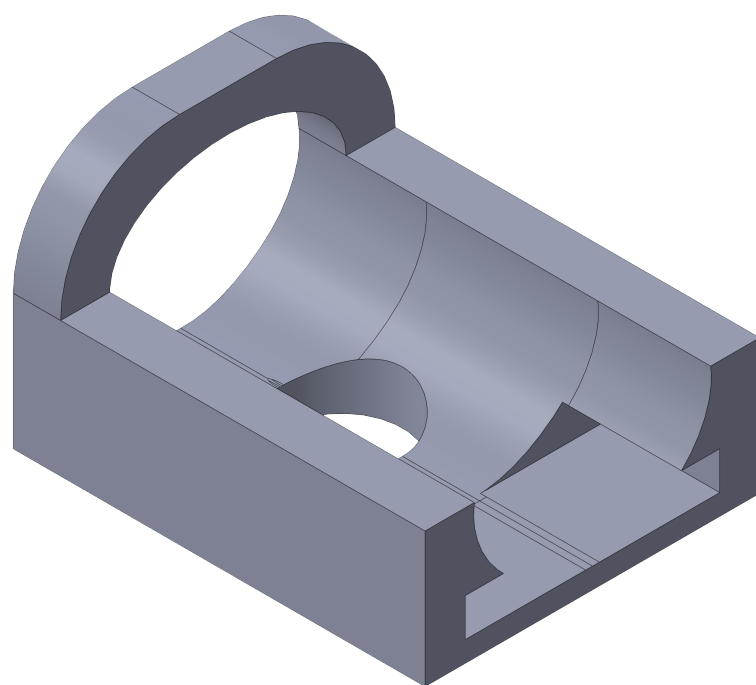


FIGURE 5.14: Silicon finger sleeve holder

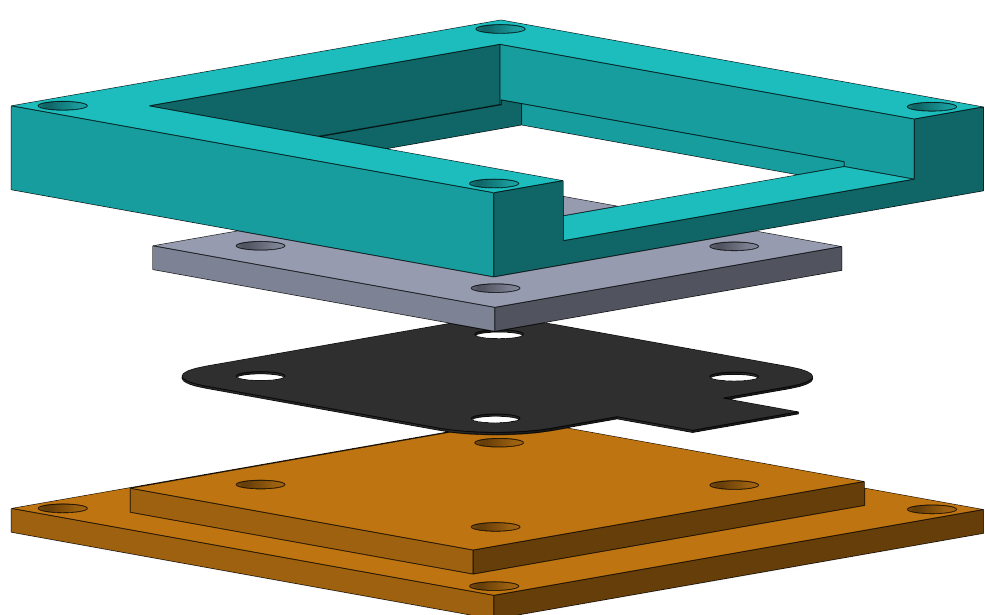


FIGURE 5.15: Explode of the coil trap

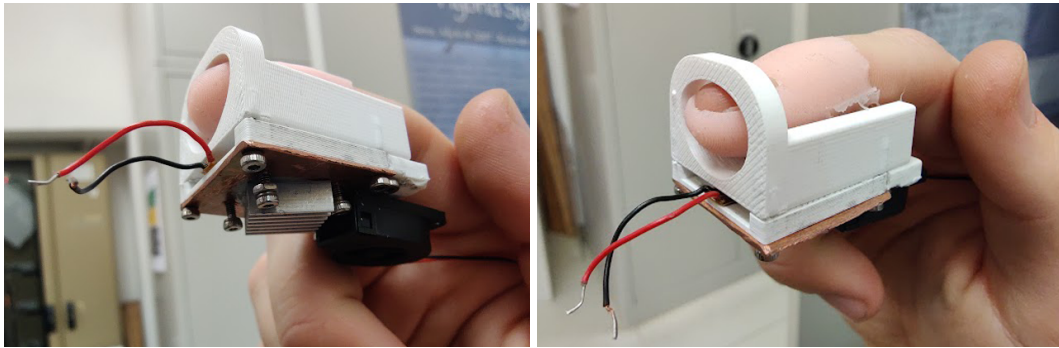


FIGURE 5.16: Bottom and top view of the real prototype

Heat dissipation

As the coil while active produces a lot of heat, we decided to introduce a heatsink in the design (the part in bronze in figure 5.15). The heatsink was made by cutting two small strips from a thin sheet of copper (1mm thick) that are joined together by thermal paste and screws. The same screws are also used to keep in place the coil and the coil holder.

For the same heat dissipation reason, we printed all components in ABS as it has a higher melting point than PLA.

Prototype usability

This prototype was much more usable than the previous one. The magnet was also kept at the right distance from the coil and the vibrations were much more noticeable, also being wearable made it much easier to use. The biggest problem of this prototype was the silicon sleeve, as the silicon tends to absorb some of the vibrations produced by the coil and the softness of the material made the mounting mechanism a bit finicky. We also had to add a small blowing fan and another part to the heatsink (as we can see in figure 5.16) to keep the coil cool as it would heat a lot after a few minutes of use.

5.3 Flexible Mat Prototypes

The goal of these prototypes was to create a small silicone mat where the magnet could be suspended in a membrane integrated into the mat itself. The coil and its heatsink would also be "trapped" inside the mat. As the mat would be made of silicone, it would allow the device to flex with the flexible coil. As we can't 3D print silicone we had to create the entire design to be able to make it by silicone casting taking into account all the design limitations of this method. All the pieces were designed in SolidWorks and then 3D printed to create the molds for the silicone casting.

5.3.1 Design of the membrane

The design goal for the membrane was to create a structure that could support the magnet just enough to win over its gravitational force so that any other force applied to it on the z-axis would be enough to move it and make it vibrate. For the membrane design, we decided to use a simple Celtic-cross structure as we described previously

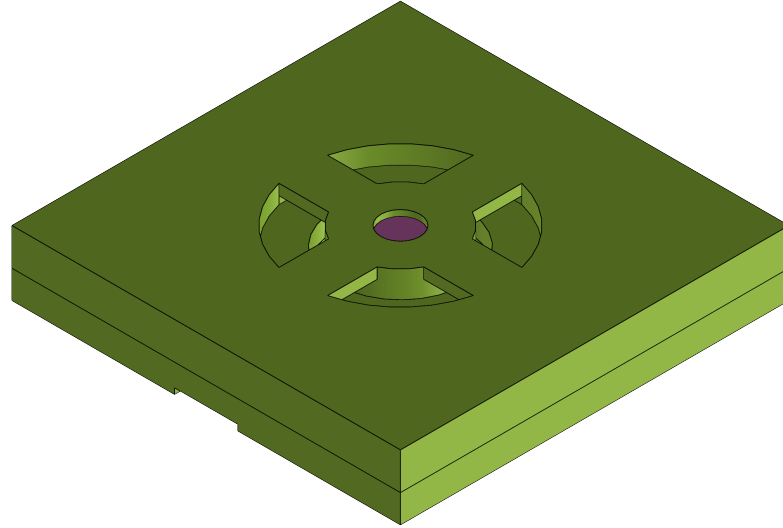


FIGURE 5.17: Membrane virtual model of the small magnet prototype.

in section 2.4.3. This resulted in a membrane with a central cylindrical chamber used to trap the magnet which is suspended by four parallelepipedal arms.

Material stiffness and thickness

While prototyping we experimented with the same two different silicone materials we described in section 5.2.2. We quickly realized that the softer silicone was too soggy as the membrane arms would need to be too thick to support the magnet. We so decided to move forward with only the harder silicone which allowed us to create thinner arms.

Membrane structure vs magnet dimensions

The main prototypes we realized were designed with two different N52 cylindrical magnets in mind. The first one is a small 10mm diameter and 2mm thick magnet, the second one is a 15mm diameter and 3mm thick magnet. The two magnets also have very different weights, the small one weighs 1.13g while the big one 4.03g. The first design of the membrane was based on the small magnet, thanks to it being lightweight it could be supported by a membrane with very thin arms (0.6mm) and a width of 4mm. The membrane arms needed also to be long enough to allow the magnet to move freely on the z-axis, so we decided to make them 4mm long.

Switching to the big magnet we realized that the membrane arms would need to be thicker to support the magnet, even if we made them wider (5mm). This was due to the increased weight of the magnet and the increase in the arms' length (now 5mm) we needed to make to allow the magnet to move freely on the z-axis. To find the minimal thickness we used the model described in subsection 2.4.3. We set a maximum deflection of 0.8mm for the membrane arms and calculated the thickness needed to support the magnet using equations 2.39 and 2.40. The results showed

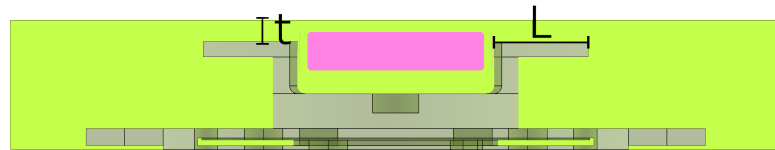


FIGURE 5.18: Membrane cross-section of the small magnet prototype
(t ->thickness, L ->length).

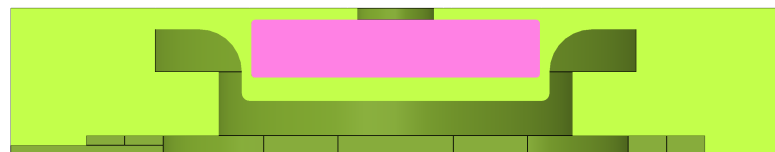


FIGURE 5.19: Membrane cross-section of the big magnet prototype.

that the membrane arms would need to be at least 1.45mm thick to support the magnet, so we decided to make them 1.6mm thick to have a safety margin.

The next problem we encountered arose when we observed that the membrane arms were breaking at the connection with the cylindrical chamber. This was the abrupt change of profile that was causing a stress concentration at that point. To solve this problem we decided to add a small fillet to the connection between the arms and the chamber.

5.3.2 Design of the mat

The mat structure is based on a simple idea but its design was quite complex to be realized with silicon casting. This is mostly due to our goal of integrating the membrane into the mat itself. This is due to our design goals:

- The membrane and magnet need to be integrated into the mat structure.
- There needs to be a mechanical way to keep the coil and its heatsink steady inside the silicone structure of the mat, as nothing can be glued to silicone.
- We need to create a channel for the magnet chamber to move freely on the z-axis.
- The complete structure must be able to flex somewhat.

As the silicon sleeve of the previous prototype 5.2.2 we opted for a two-part mold to create the mat:

- **Mold cavity:** The cavity was designed as a parallelepipedal empty box to create a simple parallelepipedal external structure for the mat. The purple com-

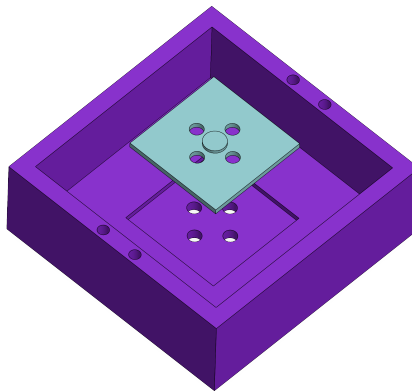


FIGURE 5.20: Flexible mat mold cavity

ponent in figure 5.20 has four screw holes at the top to screw the suspended core to the cavity. The cavity also has a rectangular hole at the bottom where the small component in light blue is inserted. This component function is to work as a pedestal for the magnet, its exact function will be explained in the next section.

Through both components are carved four holes, these are used to allow the excess silicone of the casting process to flow out of the cavity.

The purple part was 3D-printed in a flexible material called TPU to allow the mat to be easily removed from the cavity.

- **Mold core:** The core is composed of multiple components that are inserted into the cavity to create the internal structure of the mat. In figure 5.12 we can see all the components of the core, which are:
 - **Mold core center** (in light blue) : This is the central component of the core, it is used to create the coil membrane and the channel for the magnet chamber to move.
 - **Coil trap** (in red) : This is the structure that will house the coil and its heatsink and the only part of the core that will remain inside the mat.
 - **Mold core cap** (in yellow) : This component is used to keep the coil trap in place and to prevent the silicone from entering the coil trap.
 - **Mold core - cavity bridge** (in pink) : This part screws into the core and the cavity to keep the core suspended in the cavity.

Magnet chamber and membrane

To create the membrane and trap the magnet inside its chamber we needed a way to allow the silicone to flow all around the magnet. To create the upper part of the chamber we modeled the mold core center to have a cylindrical hole in its center, deep and large enough to create a silicone wall around the magnet with a lateral thickness of 0.5mm and a bottom thickness of 1.2mm. To cast the upper part of the chamber we created a pedestal (the light blue component in figure 5.20) for the magnet to rest on, the pedestal is a simple rectangular structure with a small circular

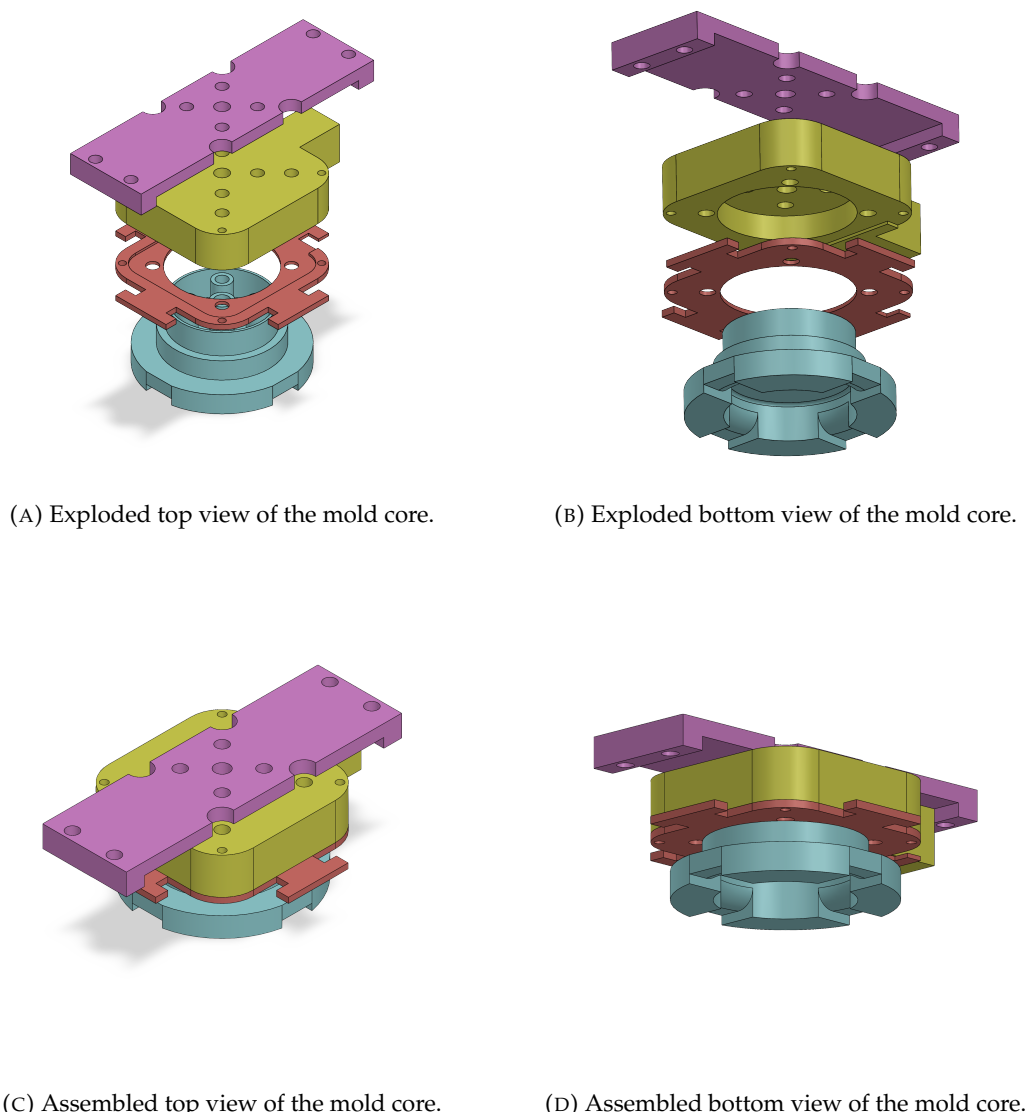


FIGURE 5.21: Assembly of the mold core

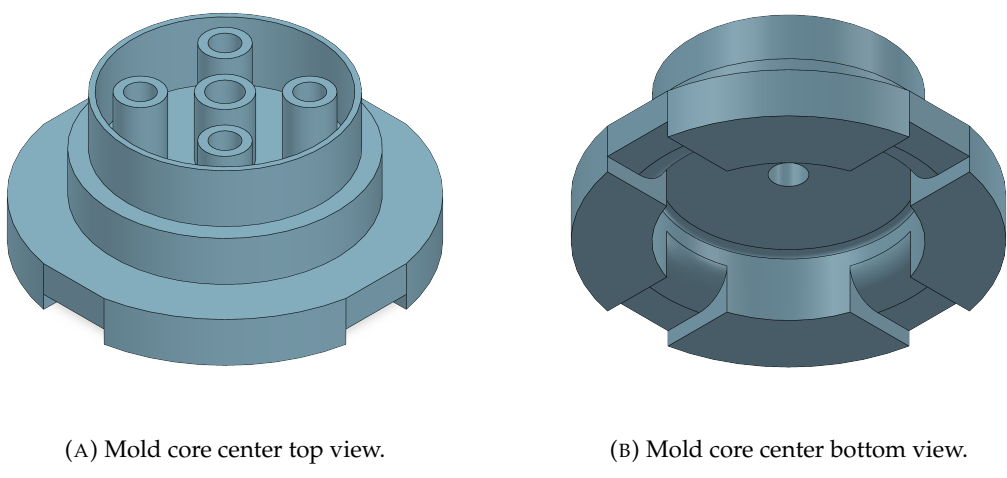


FIGURE 5.22: Mold core center.

bump at its center where the magnet is glued on. When the silicone is set the pedestal can be removed and the magnet will be trapped inside the chamber by an upper silicone ceiling of thickness 0.6mm. The curved parts and the square holes we can see in figure 5.22 are used to create the membrane arms.

The part used to create the channel is composed of three different-sized cylinders, the first one (the largest) is used to create the space for the membrane arms to flex, the second one is used to create the channel itself and the third one is used as a support for the coil trap and cap to be imbed onto it.

On the top, the center component presents four holes that are used to screw it onto the cap and one larger central one that reaches through up to the magnet surface which is used to pour the silicone into the chamber.

When the silicone is set the core center would remain stuck into the mat as it is too complex to be removed without damaging the mat itself. To solve this problem we decided to create the core center in a material that could be easily dissolved in water. This material is called BVOH and is a water-soluble filament that can be used as a support material for 3D printing. To speed up the dissolution process we decided to print the core center with low infill and shave some material off the smallest cylinder to allow the water to reach the BVOH more easily.

Distance magnet-coil

The middle cylinder is what dictates the distance between the magnet and the coil. This distance is crucial as it will determine the strength of the magnetic field that will reach the magnet. After multiple prototypes, we landed on a distance of 3.5mm between the magnet and the coil. In theory, the distance could be lower but we had to take into account the flexing of the membrane due to the pressure on it generated by the finger grasping the device.

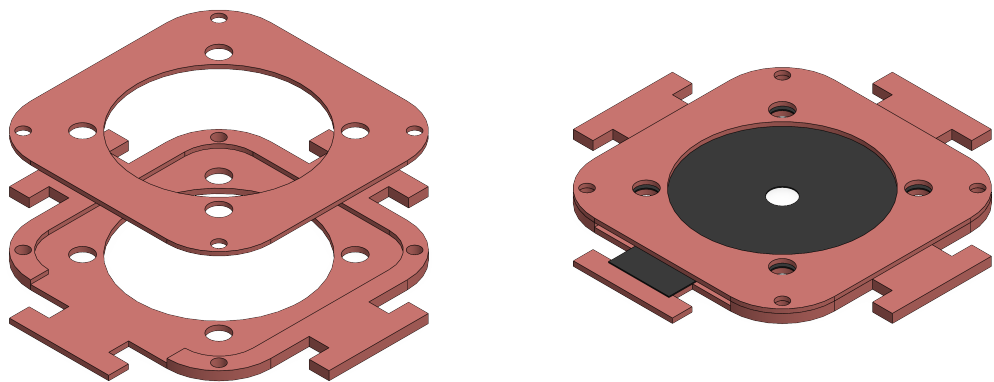
Coil trap

This component has two functions, the first one is to house the coil and its heatsink and the second one is to trap the coil mechanically inside the mat. Our main design limitations were that we couldn't glue the trap to the mat and that the trap needed to be able to flex with the mat and coil. The design we came up with is a thin square structure with a small higher border where the coil is positioned (the lower part in figure 5.23). The coil is then covered by a thin square plate that is screwed to the trap (the higher part in figure 5.23). On the side of this square, we have four thin fins that will remain inside the silicone structure of the mat, mechanically blocking the trap inside. As the coil trap is very thin and it's printed in TPU it can easily flex with the mat and the coil.

Production method

To create a new mat various steps need to be followed:

- **Components printing:** All the components of the core and the cavity need to be printed.
- **Cavity assembling:** We first need to glue the magnet to the pedestal and then place it inside the hole at the bottom of the big part.



(A) Coil trap exploded view.

(B) Coil trap with coil closed view.

FIGURE 5.23: Coil trap model.

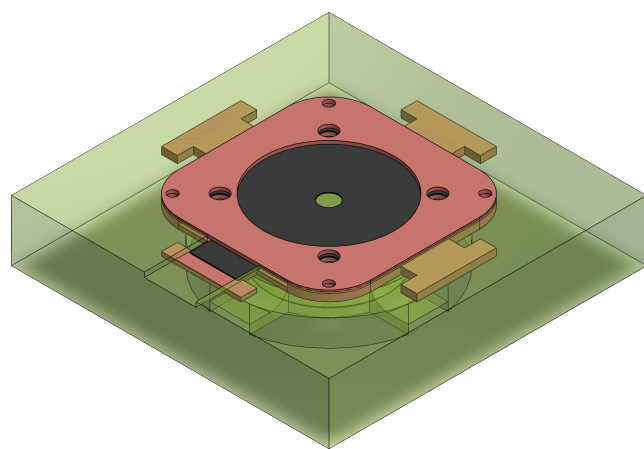


FIGURE 5.24: Coil trap placed inside the mat.

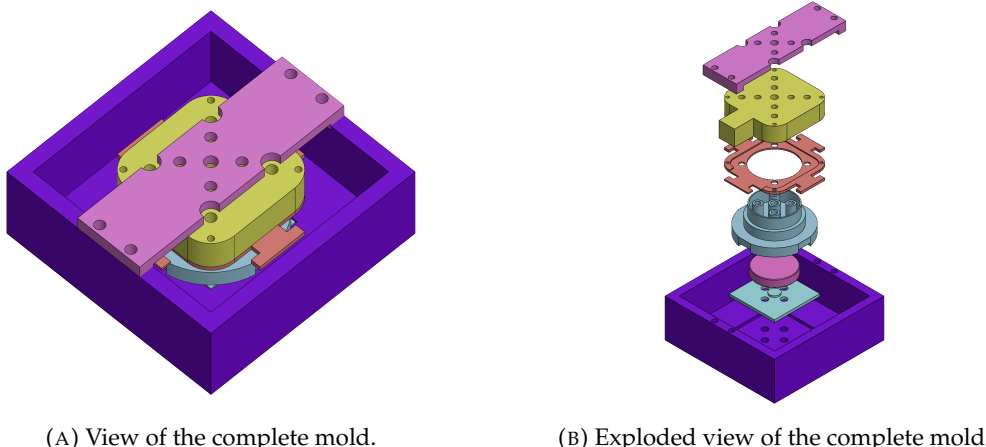


FIGURE 5.25: Complete mold for the mat.

- **Core assembling:** We start by placing the bottom part of the coil trap on the smallest cylinder of the core center, then we screw the mold core cap and bridge to the core center and finally we screw the bridge to the cavity.
- **Silicone casting:** We mix the silicone and pour it first into the big hole on top of the cap with a syringe until the chamber is filled, we can notice when it's full by observing the holes at the bottom of the cavity and the membrane holes on the core center. We then pour the rest of the silicone into the cavity until the silicone covers the coil trap fins.
- **Removing the mat from the mold:** After the silicone is set we can remove the mat from the mold by unscrewing the bridge and pulling it out. Now we can also remove the pedestal and core cap.
- **Removing the core center:** We then place the mat in a container filled with water and let it dissolve the core center.
- **Finalizing the mat:** After the core center is dissolved we can place the coil with its heatsink inside the trap and screw the cover on.

Different prototypes required some different additional clean-up steps to remove some silicone excess.

5.3.3 Design faults and problems

Membrane fragility

As we previously touched on in paragraph 5.3.1, the membrane arms tend to break at the connection with the cylindrical chamber. This is due to the abrupt change of profile that causes a stress concentration at that point. This problem was especially noticeable during testing, as we had to remove the magnet from the chamber multiple times damaging the structure of the membrane. Adding some fillets to the connection between the arms and the chamber helped to solve this problem, but it didn't eliminate it. The good thing is that the membrane is easily fixable by adding very small amounts of silicone to the broken parts as glue and letting it cure.

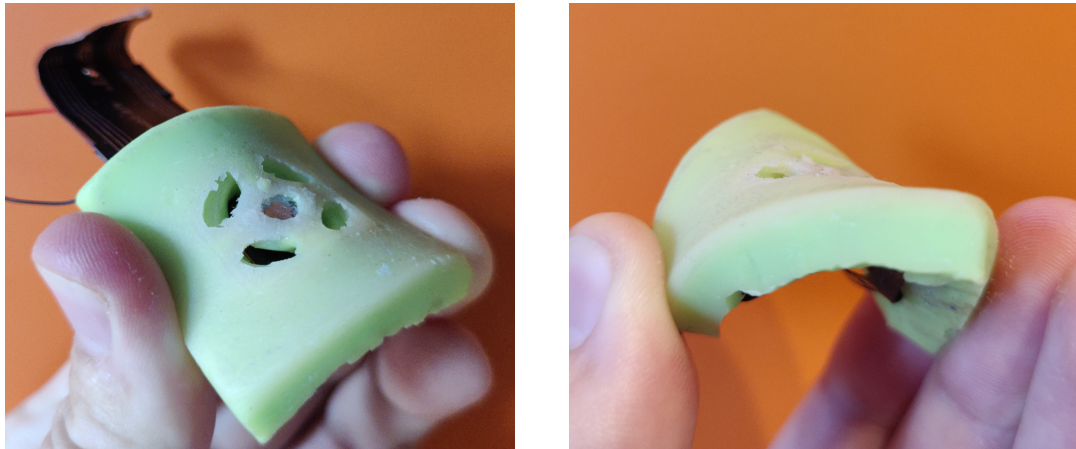


FIGURE 5.26: Flexible mat prototype bending.

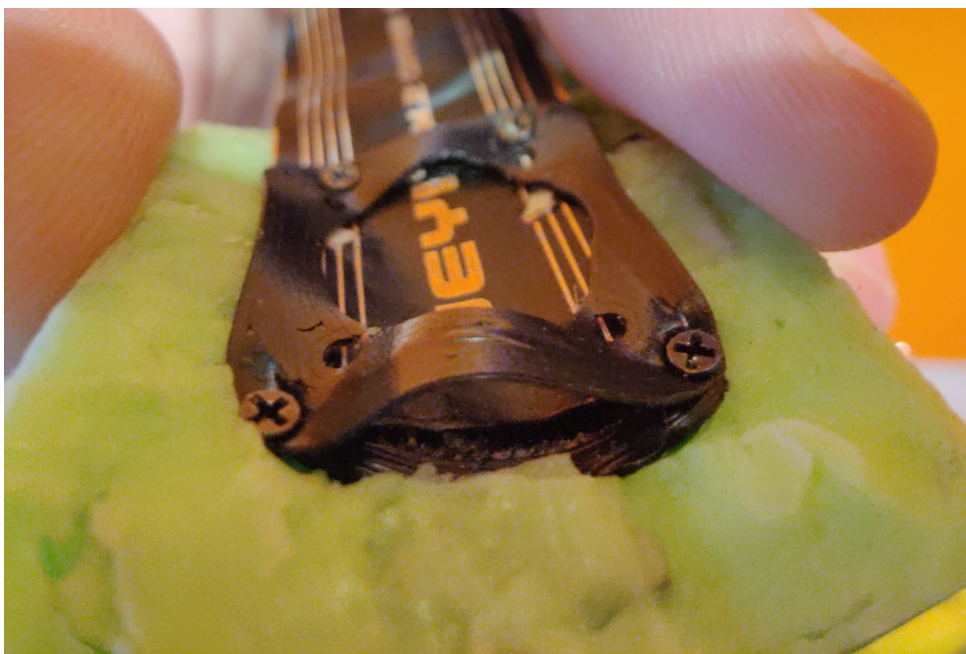


FIGURE 5.27: Coil trap separating when the mat is bent.

Overall system flexibility

In the case of the small magnet, this design resulted in a pretty flexible device that could be bent a fair amount in all directions.

Meanwhile, in the case of the big magnet, the mat was also pretty flexible but the magnet with its size impeded the structure from bending as much as the small magnet version.

Coil trap design faults

The main problem with the coil trap design was that screwing the two parts together is not reliable. As the two parts are connected by screws in only four points they tend to separate when the mat is bent. This is because the lower part follows the bending of the mat through its fins, these fins are not directly connected to the upper part.

5.4 Experimentation and Evaluation

5.4.1 Heating testing

Single coil in DC

Single coil in AC [-V, V]

Single coil in AC [0, V]

Two coils in parallel DC

Two coils in parallel AC

5.4.2 Magnet size vs Force

5.4.3 Force vs number of coils

5.4.4 Voltage vs Force

Chapter 6

Discussion and conclusions

6.1 Challenges in On-Board AI Systems for Space Missions

AI algorithms in on-board space applications encounter significant challenges related to both verifiability and computational load, crucial factors for the success and safety of space missions.

6.1.1 Verifiability Issues

AI algorithms, particularly those employing deep learning, are characterized by intricate architectures and numerous parameters. The complexity of these models makes it challenging to provide comprehensive assurance of their correctness. In space applications, where system failures are not an option, ensuring the verifiability of AI algorithms becomes predominant.

Many AI models, including deep neural networks, lack inherent explainability. Understanding the decision-making process within these "black box" models is essential to verify their reliability. Achieving transparency in AI decision logic is critical in scenarios where the basis for decision-making must be interpretable, such as during critical space maneuvers.

Space environments are dynamic and may exhibit uncertainties. AI algorithms designed for adaptability and learning might introduce challenges in predicting their behavior accurately. Verifying the robustness of adaptive AI systems in the face of unforeseen conditions is a persistent concern.

6.1.2 Computational Issues

On-board space systems typically operate with limited computational resources due to factors such as size, weight, and power constraints (SWaP). Implementing AI algorithms with demanding computational requirements may strain available resources, affecting the overall efficiency of the system.

Certain space applications, such as autonomous navigation or hazard avoidance, demand real-time decision-making. AI algorithms with high computational loads may struggle to meet these stringent timing constraints. Delays in processing could lead to missed opportunities or, in critical situations, mission failure.

In addition to computational power, energy efficiency is a crucial consideration. Prolonged missions and the reliance on energy-harvesting sources necessitate AI algorithms that balance computational complexity with energy consumption, ensuring sustained and reliable operation.

Addressing these challenges requires a multidisciplinary approach involving AI researchers, space engineers, and mission planners. Techniques such as formal verification, explainable AI, and hardware optimization are essential to enhance the verifiability and efficiency of AI algorithms in on-board space applications.

6.2 Results Analysis

In the broader context, the multi-model configuration emerges as the more robust and adaptable option, showcasing superior performance on the test set and demonstrating effective generalization capabilities to previously unseen data. The overall system score on the test dataset is $S = 0.0447$, primarily affected by the translation component $S_T = 0.0390$, as opposed to the relatively lower contribution from the rotation aspect, $S_R = 0.0057$. The noteworthy aspect is the necessity of prioritize the minimization of translation errors, since, in proximity to the target, precise translation is crucial for accurate maneuvering. Moreover, rotation pose can be more effectively predicted with the incorporation of a navigation filter. This strategic integration allows for a corrective mechanism, compensating for rotational discrepancies and enhancing the system's overall precision in navigating close quarters.

6.3 Possible Improvements

Another option would be using multiple models also for the *Landmark Regression* module, which are able to identify a target set of landmarks in farther positions and a second set in closer distances to the target, in order to keep the number of identified points in the image frame as greater as possible.

This implementation would also lead to a more accurate pose estimation in positions closer to the minimum distance analyzed in the experiments (from $40cm$ to $20cm$). A well-performed pose estimation in positions very close to the target would help to minimize any errors introduced by camera distortions.

6.3.1 Landmark Mapping Sensitivity

The assessment of trajectories such as *Less_Difficult_Trajectory* and *Difficult_Trajectory* is conducted with a noteworthy consideration: the assumption of zero prediction error for the points' location in the image. This assumption is made out of necessity since the *Landmark Regression* module encounters difficulties in identifying all the landmarks expected to be present in the image frames. Consequently, the input data for the *Landmark Mapping* module is marked by a heightened sensitivity, as the accuracy of its predictions is contingent upon the successful identification of landmarks by the preceding module.

A potential avenue for improvement involves an expansion of the training dataset to incorporate instances where certain landmarks remain unidentified due to inherent challenges in their recognition. This strategy aims to enhance the model's resilience to scenarios where specific landmarks pose persistent issues during identification. By exposing the model to a more diverse range of challenges and including cases of landmark ambiguity, it is anticipated that the trained model will develop a more robust understanding, leading to improved performance, particularly in situations mirroring real-world complexities. This adjustment aligns with the overarching goal of fortifying the system's adaptability and generalization capabilities, addressing

challenges posed by varying environmental conditions and unforeseen factors during autonomous space applications.

Moreover, to fortify the robustness of the system, there is a prospect to introduce a more sophisticated pre-processing system. This advanced system would be designed to mitigate the impact of varying image light conditions on landmark identification. By incorporating techniques such as adaptive image enhancement, contrast normalization, or even exploring deep learning-based methods for illumination invariance, the model could become less susceptible to fluctuations in lighting. Such enhancements would foster greater reliability in landmark identification by the *Landmark Regression* module, subsequently improving the overall accuracy of the *Landmark Mapping* module. This proactive approach anticipates and addresses challenges associated with real-world scenarios where illumination conditions can be unpredictable, ensuring the model's effectiveness across diverse operational environments in on-board space applications.

6.4 Conclusions

This project presents a dedicated monocular pose estimation framework designed for spaceborne objects, emphasizing its applicability to satellite rendezvous maneuvers. The framework capitalizes on the strengths of deep neural networks, seamlessly integrating feature learning and establishing robust 2D-3D correspondence mapping. Notably, the incorporation of HRNet, known for its high-resolution image representation, significantly contributes to the precision of pose predictions and the subsequent refinement process. The framework further demonstrates its efficiency by employing geometric optimization techniques, ensuring accurate alignment of point sets and enhancing the overall robustness of the pose estimation system.

Appendix A

Support Code

A.1 Ground Truth Heatmaps

```

1 import numpy as np
2
3 def createHeatmap(landmark, vp, hmap_w, hmap_h, sig=1):
4     hmap = np.zeros((hmap_height + 3, hmap_width + 3))
5     x, y = landmark
6     if vp:
7         for i in range(y - 3*sig, y + 3*sig):
8             for j in range(x - 3*sig, x + 3*sig):
9                 hmap[i,j] += np.exp(-((i-y)**2 + (j-x)**2)/(2*sig**2))
10
11    hmap = hmap[1:-2, 1:-2]
12
13    return hmap
14
15 def coord2Heatmap(landmarks, vis, hmap_w=512, hmap_h=512, sig=1):
16     hmaps = []
17
18     for landmark, vp in zip(landmarks, vis):
19         hmaps.append(createHeatmap(landmark, vp, hmap_w, hmap_h, sig))
20
21     hmaps = np.array(hmaps).squeeze()
22
23     return hmaps

```

LISTING A.1: Ground Truth Heatmaps

A.2 Landmark Location Selection

```

1 import numpy as np
2
3 def get_landmarks(landmarks_images, threshold1=-0.5, threshold2=-0.6):
4     landmarks2D = []
5     for img in landmarks_images:
6         Lnd_found = False
7         lndx = -1
8         lndy = -1
9         mask1 = img < threshold2
10        img[mask1] = -1
11
12        if np.max(img) > threshold1:
13            Lnd_found = True
14        elif np.max(img) > threshold2 and np.var(img) > 2e-6:
15            Lnd_found = True
16
17        if Lnd_found:
18            p_lndy, p_lndx = np.where(img == np.max(img))
19            lndx = np.round(np.mean(p_lndx))
20            lndy = np.round(np.mean(p_lndy))
21            if landmarks2D is not None or len(landmarks2D) > 0:
22                for data in landmarks2D:
23                    if data[2] == 1 and abs(lndx - data[0]) <= 3
24                        and abs(lndy - data[1]) <= 3:
25                            if np.max(img)>data[3] and np.var(img)>data[4]:
26                                data[0] = -1
27                                data[1] = -1
28                                data[2] = 0
29                                n_lnd=[lndx,lndy,1,np.max(img),np.var(img)]
30                            else:
31                                n_lnd = [-1,-1,0,np.max(img),np.var(img)]
32
33                n_lnd = [lndx,lndy,1,np.max(img),np.var(img)]
34            else:
35                n_lnd = [-1,-1,0,np.max(img),np.var(img)]
36
37            landmarks2D.append(n_lnd)
38
39    return np.array(landmarks2D)

```

LISTING A.2: Landmark Location Selection

Bibliography

- [1] Carl Bugeja. *LinkedIn Profile*. <https://www.linkedin.com/in/carl-bugeja-0b922a135/>. Accessed: 2024-05-27. 2024.
- [2] corz.org. *ESP32 Signal Generator*. <https://corz.org/ESP32/square-sine-triangle-wave-signal-generator>.
- [3] Nicole D'Aurizio. "Algorithms and Wearable Technologies Enabling Haptic Communication". Available at <https://hdl.handle.net/11365/1225277>. PhD thesis. University of Siena, Jan. 2023.
- [4] Martin Geier et al. "Mathematical Modeling of an Electromagnetic Forming System with Flat Spiral Coils as Actuator". In: (Jan. 2010). DOI: 10.17877/DE290R-14276.
- [5] HZDR. *HZDR - Helmholtz-Zentrum Dresden-Rossendorf*. <https://www.hzdr.de>.
- [6] Peter Johnson and Janet Blackstone. "Children and gender - Differences in exposure and how anthropometric differences can be incorporated into the design of computer input devices". In: *SJWEH Supplements* 33 (Jan. 2007).
- [7] K. Kawabe, H. Koyama, and K. Shirae. "Planar inductor". In: *IEEE Transactions on Magnetics* 20.5 (1984), pp. 1804–1806. DOI: 10.1109/TMAG.1984.1063271.
- [8] A. Khurshid, Abdul Ghafoor, and Afzaal Malik. "Robotic Grasping and Fine Manipulation Using Soft Fingertip". In: Aug. 2011. ISBN: 978-953-307-373-6. DOI: 10.5772/23697.
- [9] L272: *Dual Power Operational Amplifier*. L272. STMicroelectronics. 2003. URL: <https://www.st.com/resource/en/datasheet/l272.pdf>.
- [10] Dr. Minas E. Lemonis. *Statics of fixed beams*. <https://calcresource.com/statics-fixed-beam.html>.
- [11] microbots. *microbots Company*. <https://www.microbots.io>.
- [12] Minh Nguyen and Handy Blanchette. "Optimizing AC Resistance of Solid PCB Winding". In: *Electronics* 9 (May 2020), p. 875. DOI: 10.3390/electronics9050875.
- [13] Christian Østergaard et al. "Simulation and measurement of AC resistance for a high power planar inductor design". In: *2019 IEEE 13th International Conference on Compatibility, Power Electronics and Power Engineering (CPE-POWERENG)*. 2019, pp. 1–5. DOI: 10.1109/CPE.2019.8862361.
- [14] Stefano Papetti et al. "Vibrotactile Sensitivity in Active Touch: Effect of Pressing Force". In: *IEEE Trans. Haptics* 10.1 (Jan. 2017), pp. 113–122. ISSN: 1939-1412. DOI: 10.1109/TOH.2016.2582485. URL: <https://doi.org/10.1109/TOH.2016.2582485>.
- [15] *Piezo Haptic Actuator - PowerHap*. PowerHap 15G. TDK. 2017. URL: https://www.mouser.com/datasheet/2/400/PowerHap_15G-1144538.pdf.
- [16] piezodrive.com. *Piezo Actuator Power Calculator*. <https://www.piezodrive.com/piezo-actuator-power-calculator/>.
- [17] ResChimica. *R Pro 10 Silicon*. <https://www.reschimica.com/it/gomme-siliconiche/121-227-r-pro-10-gomma-siliconica-liquida-per-stampi-morbidi.html>.

- [18] ResChimica. *R Pro Fast Silicon*. <https://www.reschimica.com/it/gomme-siliconiche/119-222-r-pro-fast-gomma-siliconica-per-prototipazione-rapida.html>.
- [19] supermagnete.de. *Magnetic field of various permanent magnets*. <https://www.supermagnete.de/eng/faq/How-do-you-calculate-the-magnetic-flux-density>.
- [20] The Engineering ToolBox. *Length of a Spiral*. https://www.engineeringtoolbox.com/spiral-length-d_2191.html [Accessed: 22/04/2024]. 2021.
- [21] John Wu et al. "Finite element analysis of the penetrations of shear and normal vibrations into the soft tissues in a fingertip". In: *Medical engineering & physics* 29 (July 2007), pp. 718–27. DOI: 10.1016/j.medengphy.2006.07.005.
- [22] Jonsenser Zhao. "A new calculation for designing multilayer planar spiral inductors". In: *Edn -Boston then Denver then Highlands Ranch Co-* 55 (July 2010), pp. 37–40.

Acknowledgements

Desidero esprimere i miei più sentiti ringraziamenti a tutte le persone che hanno contribuito al completamento di questa tesi.

Innanzitutto, desidero ringraziare il mio relatore, il prof. Marcello Chiaberge, e co-relatore, l'ing. Andrea Merlo, per avermi dato la possibilità di intraprendere questo progetto. Ringrazio l'ing. Marco Lapolla per la sua guida, disponibilità e dedizione nell'aiutarmi a sviluppare e perfezionare il mio lavoro.

Un ringraziamento speciale va alla mia famiglia che ha sempre sostenuto e incoraggiato il mio percorso accademico. Il loro sostegno e supporto sono stati la spinta necessaria per superare le sfide e raggiungere questo traguardo.

Ringrazio i compagni dell'università: Vale, Ali, Morgan, Matte, Nicoli, Franco, Luca e Nicco, che hanno alleviato le mie giornate e contro cui ho perso innumerevoli partite a bodriga.

Un ringraziamento agli amici di FORO, mia casa nell'ultimo periodo, con cui ho condiviso molte pause caffè.

Agli amici di una vita e compagni di mille avventure: Gian, Pier, Ale, Stol, Lollo e Chiara che, nonostante le nostre strade stiano prendendo direzioni diverse, sono e saranno sempre presenti al mio fianco.

Infine, il ringraziamento più importante va a Nau, mia compagna di viaggio, che mi ha sostenuto in questo percorso, credendo in me anche quando io non l'ho fatto.

Grazie mille a tutti.

Fede